Mathematical and computational modelling of spatio-temporal signalling in rod phototransduction

G. Caruso, H. Khanal, V. Alexiades, F. Rieke, H.E. Hamm and E. DiBenedetto

Abstract: Rod photoreceptors are activated by light through activation of a cascade that includes the G protein-coupled receptor rhodopsin, the G protein transducin, its effector cyclic guanosine monophosphate (cGMP) phosphodiesterase and the second messengers cGMP and Ca^{2+}. Signalling is localised to the particular rod outer segment disc, which is activated by absorption of a single photon. Modelling of this cascade has previously been performed mostly by assumption of a well-stirred cytoplasm. We recently published the first fully spatially resolved model that captures the local nature of light activation. The model reduces the complex geometry of the cell to a simpler one using the mathematical theories of homogenisation and concentrated capacity. The model shows that, upon activation of a single rhodopsin, changes of the second messengers cGMP and Ca^{2+} are local about the particular activated disc. In the current work, the homogenised model is computationally compared with the full, non-homogenised one, set in the original geometry of the rod outer segment. It is found to have an accuracy of 0.03% compared with the full model in computing the integral response and a 5200-fold reduction in computation time. The model can reconstruct the radial time-profiles of cGMP and Ca^{2+} in the interdiscal spaces adjacent to the activated discs. Cellular electrical responses are localised near the activation sites, and multiple photons sufficiently far apart produce essentially independent responses. This leads to a computational analysis of the notion and estimate of 'spread' and the optimum distribution of activated sites that maximises the response. Biological insights arising from the spatio-temporal model include a quantification of how variability in the response to dim light is affected by the distance between the outer segment discs capturing photons. The model is thus a simulation tool for biologists to predict the effect of various factors influencing the timing, spread and control mechanisms of this G protein-coupled, receptor-mediated cascade. It permits ease of simulation experiments across a range of conditions, for example, clamping the concentration of calcium, with results matching analogous experimental results. In addition, the model accommodates differing geometries of rod outer segments from different vertebrate species. Thus it represents a building block towards a predictive model of visual transduction.

1 Introduction

An important goal of modern biology is to predict cellular behaviours as a function of complex inputs. It is well known that regulatory interactions in cellular signalling cascades are highly localised and thus cannot be modelled

using 'well-stirred' assumptions of ordinary differential equations. Computationally less tractable partial differential equations are needed to capture the spatio-temporal evolution of signalling cascades. Thus more sophisticated mathematical and computational methods are needed to describe them accurately. The significance of this paper is its introduction of a mathematical technique that simplifies the computation of the spatial spread of second messengers and other diffusing species. This approach is used to describe the diffusion of cyclic guanosine monophosphate (cGMP) in visual transduction.

Phototransduction is the process by which photons of light generate, by activating a biochemical cascade, an electrical signal in a rod outer segment (ROS), thereby initiating the process of vision. This process is mediated by the diffusion of the second messengers cGMP and Ca^{2+} (calcium ions) in the cytoplasm of the ROS.

Phototransduction is among the best-understood signalling processes, with the underlying biochemistry, geometry and basic physics known in some detail. Thus it is a prime candidate for detailed quantitative modelling. Great strides were made over the past decade in developing basic models for the time-evolution of

IEE Proc.-Syst. Biol., Vol. 152, No. 3, September 2005

119

the response [1, 2], by viewing the ROS as a single, well-stirred compartment.

The next natural stage is to develop spatio-temporal models accounting for diffusion of second messengers in the cytoplasm. Such models should display all the spatial localisation effects characterising the rod phototransduction signalling process and enable the prediction of quantities that are difficult or impossible to measure experimentally, such as longitudinal and radial profiles of concentrations, their longitudinal spread, the magnitude of response at the activation site (expected to be much higher than the overall, integral response), and how the response might be affected by how far apart photons happen to be absorbed.

There is an intrinsic difficulty in describing this diffusion efficiently, owing to the intricate, layered geometry of the ROS. The space available for diffusion consists of thin, horizontal cytoplasmic layers connected by a vertical, cylindrical space of comparable thickness, as in Fig. 1. We can formulate a pointwise model (Section 2.2) of such a diffusion process, based on Fick's law, by regarding each layer as a thin but three-dimensional region [3–6]. Although the numerical and computational analysis is greatly complicated by such a structured geometry, the model has the advantage of expressing the physics of the phenomenon locally. We call this the full three-dimensional model.

Andreucci *et al.* [3, 4] suggested an approach to eliminate the geometrical complexity of the ROS using the mathematical processes of homogenisation and concentrated capacity. By this process, the 'homogenised' ROS becomes a cylinder with no layers, and the 'homogenised' Fick's diffusion is recast in terms of an 'interior' diffusion, within such a cylinder, augmented by a diffusion process taking place on the lateral boundary of such a limiting ROS. We shall refer to it as the homogenised model (Section 2.3).

The homogenisation technique is mathematically elegant, and the associated computational analysis is considerably simplified. However, the homogenisation process removes any intuitive connection with the underlying physics, and it is natural to ask whether the homogenised model produces results close to the original full three-dimensional model. This is precisely the scope of the present paper.

Numerical simulations of the response of dark-adapted salamander rods to dim light flashes are performed with both models, and their results are numerically compared (Section 3). In the simulation of single photon response (SPR), the (local) 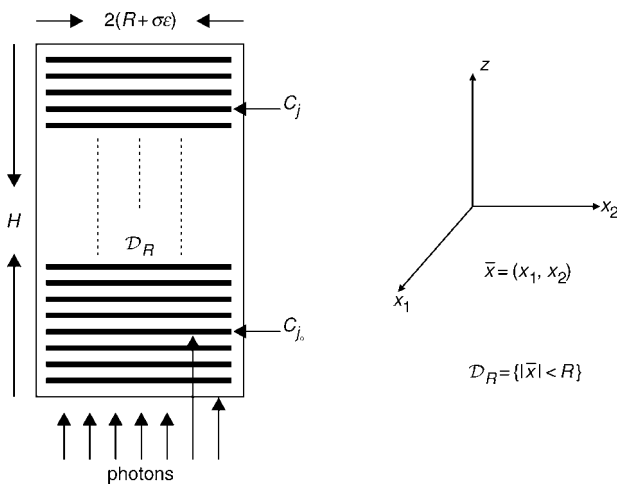concentrations $[cG]$ and $[Ca]$ predicted by the two models differ by no more than 0.2%, the corresponding local current drop differs by no more than 2%, and the total relative responses differ by no more than 0.03%. Moreover, the code for the homogenised model runs 5200 times faster than the full model.

We examine and test literature values of model parameters, identify a consistent set of parameters that yield good agreement with experimental data on salamander SPRs, thus validating the basic model, and describe in detail the localisation features of SPRs.

For multiple photon activation, we investigate how the response depends on the distribution of activation sites and identify those that yield maximum global current drop (Section 3.4). We find that the distance between ROS discs capturing photons can greatly contribute to response variability in dim light. Considerable non-linear summation of SPRs arises even with two photons.

The computational model identifies quantitatively the spread of activation, i.e. that interval, on the longitudinal axis of the ROS, about the activation site, where the response is detectable (Sections 2.1.4 and 3.2). We investigate how the spread of activation depends on D_{cG}.

This modelling approach should also be applicable to the study of the diffusion of signalling molecules in different geometries, in other cell signalling cascades.

2 Model formulation

2.1 Mechanisms of phototransduction

2.1.1 Geometry of ROS: The rod outer segment of a photoreceptor in vertebrates (Fig. 1) can be considered as a right circular cylinder Ω_ε of height H and radius R_{rod}. The cylinder contains a stack of n parallel, equispaced, disc-like, lipidic, functionally independent bilayers C_j, $j = 1, 2, \ldots, n$, each of radius R and thickness ε, mutually separated by a distance $\nu\varepsilon$, and coaxial with the cylinder Ω_ε. The gap $R_{rod} - R$ is also small, in the order of ε. We denote it by $\sigma\varepsilon$, so that $R_{rod} = R + \sigma\varepsilon$.

The bilayers C_j are called *discs* and have upper and lower faces $F_j^\pm$. The second messengers cGMP and Ca^{2+} diffuse in the cytosol, which fills that part of the ROS not occupied by the discs C_j, namely,

$$\tilde{\Omega}_\varepsilon = \Omega_\varepsilon - \bigcup_{j=1}^{n} C_j$$

This geometry implies that

$$n\varepsilon = \frac{H}{1+\nu} \quad \text{and} \quad \frac{\text{vol}(\bigcup_{j=1}^{n} C_j)}{\text{vol}(\Omega_\varepsilon)} = \frac{1}{1+\nu} \stackrel{\text{def}}{=} \theta_o \quad (1)$$

Using the co-ordinate system of Fig. 1, the lateral boundary of the ROS is described in rectangular or cylindrical co-ordinates as

$$S_\varepsilon = \{(\bar{x}, z) \mid |\bar{x}| = R + \sigma\varepsilon; z \in (0, H)\}$$
$$= \{(R + \sigma\varepsilon, \theta, z) \mid z \in (0, H), \theta \in [0, 2\pi)\} \quad (2)$$

2.1.2 Phototransduction: The plasma membrane forming the lateral boundary of the ROS contains cGMP-gated channels. In the dark, a fraction of these channels are open, permitting influx of Na$^+$ and Ca^{2+} ions. An exchanger located on the same plasma membrane extrudes Ca^{2+} and K$^+$ while permitting additional Na$^+$ influx. The exchange rate varies with internal Ca^{2+} concentration. In the dark, Ca^{2+} and cGMP are at a steady-state equilibrium,

Fig. 1 *Schematic drawing of vertebrate ROS*

and their steady-state (dark) concentrations are denoted by $[Ca]_{dark}$ and $[cG]_{dark}$. Absorption of a photon by a rhodopsin molecule residing on an outer segment disc initiates a cascade receptor → transducer → effector, whose net effect is to produce a sink (a negative source term) for cGMP produced by the activated effector PDE*. The cGMP is then depleted by flowing by free diffusion towards such a sink. Depletion of cGMP causes closing of the channels, thereby reducing the inward current. We refer to [2] for a more detailed description of such a process and to [4] for a discussion on the effects of diffusion, its localised nature and on the notion of pointwise against 'bulk' modelling.

2.1.3 Local against global currents:
The current due to Ca^{2+} exchange is given by a Michaelis Menten-type relationship

$$ J_{ex} = J_{ex}^{sat} \frac{[Ca]}{K_{ex} + [Ca]} \qquad (3) $$

where j_{ex}^{sat} is the saturated exchange current (as $[Ca] \to \infty$), and K_{ex} is the Ca^{2+} concentration at which the exchange rate is half the maximum.

At fixed membrane voltage, the current J_{cG} carried by the cGMP-gated channels is given by the Hill-type relationship

$$ J_{cG} = J_{cG}^{max} \frac{[cG]^{m_{cG}}}{K_{cG}^{m_{cG}} + [cG]^{m_{cG}}} \qquad (4) $$

where j_{cG}^{max} is the maximum cGMP-current (as $[cG] \to \infty$), m_{cG} is the Hill exponent, and K_{cG} is the binding affinity of each cGMP binding site on the channel.

These formulae are local in nature, i.e. they provide the current in terms of space-time values of $[cG]$ and $[Ca]$. As current is generated at the lateral boundary of the ROS, this is where the values of $[cG]$ and $[Ca]$ are relevant for the computation of J_{cG} and J_{ex}. In the literature, these currents are regarded as volumic, as if they were distributed over the entire ROS. In particular in [1], volumic current densities are defined by dividing the coefficients j_{cG}^{max} and j_{ex}^{sat} by the volume of the cytosol (1 picolitre).

Equations (3) and (4) imply that a local pointwise evaluation of these currents requires a pointwise description of $[cG]$ and $[Ca]$ as functions of position and time.

In the absence of light, J_{ex} and J_{cG} are constant and equal to their 'dark' values

$$ J_{ex;dark} = J_{ex}|_{t=0} = j_{ex}^{sat} \frac{[Ca]_{dark}}{K_{ex} + [Ca]_{dark}} $$
$$ J_{cG;dark} = J_{cG}|_{t=0} = j_{cG}^{max} \frac{[cG]_{dark}^{m_{cG}}}{K_{cG}^{m_{cG}} + [cG]_{dark}^{m_{cG}}} \qquad (5) $$

The local value of (total) current J_{loc} and its dark value J_{dark} are defined as

$$ J_{loc}(\theta, z, t) = J_{ex}(\theta, z, t) + J_{cG}(\theta, z, t) \quad J_{dark} = J_{loc}|_{t=0} \qquad (6) $$

As z ranges over $(0, H)$ and θ ranges over $[0, 2\pi)$, the variables (θ, z) range over the lateral boundary S_ε of the ROS. At $t = 0$, both $[Ca]$ and $[cG]$ are constant and equal to their dark values. Consequently, J_{dark} is also a constant. The local response to light activation, at time t, at a point (θ, z) of the plasma membrane, is the variation of $J_{loc}(\theta, z, t)$

from its dark value, i.e. $\{J_{dark} - J_{loc}(\theta, z, t)\}$. Set

$$ J(t) = \frac{1}{\Sigma_{rod}} \int_{S_\varepsilon} J_{loc}(\theta, z, t) dS $$
$$ J(z, t) = \frac{1}{2\pi} \int_0^{2\pi} J_{loc}(\theta, z, t) d\theta \qquad (7) $$

where Σ_{rod} is the surface area of the lateral boundary S_ε of the ROS, and dS is its surface measure. The first is the current across the entire plasma membrane at time t, averaged over S_ε; the second is the local current across the plasma membrane at some fixed level z, averaged over the z-cross-section of S_ε.

Results are presented in terms of the (total) response, $J_{dark} - J(t)$, relative response, $1 - J(t)/J_{dark}$, and relative local response, $1 - J(z, t)/J_{dark}$.

2.1.4 Spread of activation:
Let z_* be the z-location of the activated disc. At each fixed time t, the local response $J_{dark} - J_{loc}(z, t)$ is highest at $z = z_*$, it decreases symmetrically away from z_*, and it becomes 'negligible' sufficiently far away from z_*. That interval about z_*, along the longitudinal axis of the ROS where the current suppression is 'not negligible', defines, roughly speaking, the interval of spread of the response to light activation.

This localisation has been pointed out by a number of researchers [7, 8, 10–13], and it is generally accepted that the response is 'local' in the sense that the interval of spread of the response to light activation is considerably smaller than the length of the outer segment. To our knowledge, however, the literature does not contain an unambiguous quantification of 'spread' in space and time.

An intuitive way to quantify how far the response spreads, at a certain time t, would be to choose a 'reasonable' cutoff level $\delta \in (0, 1)$ and define spread of excitation as the width $\lambda(\delta, t)$ of the largest interval about z_*, along the longitudinal axis of the rod, where the response is greater than a fixed fraction δ of the dark circulating current, at that time, i.e.

$$ J_{dark} - J_{loc}(z_* \pm \lambda(\delta, t), t) > \delta J_{dark} $$
$$ \text{for a fixed } \delta \in (0, 1) \qquad (8) $$

Although the spread is a function of time, in the literature it is normally intended and estimated at the time t_{peak} of peak response. The choice of the cutoff level δ is in principle arbitrary, and we do not know of compelling physical or mathematical criteria for such a choice. However, in view of the shape of the z-profiles in Fig. 7, where the signal spreads over about 200 discs, or 4 μm, at peak time, a reasonable choice would be to take $\delta = 0.1\%$ in (8) and set

$$ \lambda_o = \lambda(10^{-3}, t_{peak}) \quad \text{identified by (8)} $$
$$ \text{for } t = t_{peak} \text{ and } \delta = 10^{-3} \qquad (9) $$

The interval of length $2\lambda_o$ about z_* is the interval of detectable response. Although the determination of such an interval is feasible in numerical simulations (see Section 3.2), it is difficult or impossible to measure experimentally, as $0.1\% J_{dark}$ is approximately 0.05 pA.

A common approach in the literature is to fit a z-profile, such as in Fig. 8, to an exponential function of the form $\exp\{-|z - z_*|/\lambda_*\}$ for some positive λ_*, and then use such a λ_*, called a spread space constant, as a way of quantifying the notion of spread at peak time. Equivalently, this

IEE Proc.-Syst. Biol., Vol. 152, No. 3, September 2005

121

can be viewed as the notion of spread, as introduced in (8), for cutoff $\delta = 1/e$, i.e.

$$\lambda_* = \lambda\left(\frac{1}{e}, t_{peak}\right) \quad \text{identified by (8)}$$

$$\text{for } t = t_{peak} \text{ and } \delta = \frac{1}{e} \qquad (10)$$

We do not know of a firm theoretical grounding for this approach. Although easier to determine experimentally, the value of the space constant does not convey the size of the interval of detectable response.

In Section 3.2, we report both quantities as obtained from our simulations, and, in Section 4.4, we present an account of the various notions of spread appearing in the literature along with various estimates for the space constant.

2.2 Full three-dimensional model

The concentrations $[cG]$ and $[Ca]$ are smooth functions of space and time, defined in the domain $\tilde{\Omega}_\varepsilon$ available for diffusion, and they satisfy the mass balance equations within such a domain. As, in the cytosol, there are no volume sources

$$\frac{\partial [cG]}{\partial t} - \nabla \cdot (D_{cG} \nabla [cG]) = 0$$
$$\hspace{4cm} \text{in } \tilde{\Omega}_\varepsilon \qquad (11)$$
$$\frac{\partial [Ca]}{\partial t} - \nabla \cdot (D_{Ca} \nabla [Ca]) = 0$$

where t is time and ∇ is the gradient in the spatial variables $(\bar{x}, z)$. The coefficients D_{cG} and D_{Ca} are the respective diffusion coefficients of cGMP and Ca^{2+} in the cytosol. For a dark-adapted rod, the initial data for the concentrations $[cG]$ and $[Ca]$ are their uniform, steady-state, dark values

$$\begin{aligned}[cG]\big|_{t=0} &= [cG]_{dark} \\ [Ca]\big|_{t=0} &= [Ca]_{dark}\end{aligned} \qquad (12)$$

2.2.1 Boundary fluxes of [cG]:
Production or depletion of $[cG]$ occurs through binding phenomena on the faces $F_j^\pm$ of the discs C_j. Accordingly, these terms are modelled as fluxes across such faces.

Basal PDE hydrolyses cGMP at all disc faces. Let $[PDE]_\sigma$ denote the surface density of PDE (in number of molecules μm^{-2}), and let $k_{\sigma;hyd}$ be the hydrolysis rate (in [numbers of molecules $\mu m^{-3}]^{-1} s^{-1}$). Accordingly, $k_{\sigma;hyd}[PDE]_\sigma$ has dimensions of $\mu m\, s^{-1}$.

The rate of cGMP depletion (per unit surface area, per unit time, i.e. depletion flux of cGMP), due to basal PDE, is given by

$$\mp k_{\sigma,hyd}[PDE]_\sigma[cG] \quad \text{on the faces } F_j^\pm \qquad (13)$$

Analogous, but volumetric, expressions appear in [8, 1], involving a volumetric hydrolysis rate k_{hyd} measured in $\mu M^{-1} s^{-1}$. A conversion factor between the two rates is sought by assuming that, in a well-stirred/bulk ROS, the same numbers of molecules of cGMP would be hydrolysed by a volumic $[PDE]$ (in μM), uniformly distributed in the cytosol, as by a surface $[PDE]_\sigma$ (in number of molecules μm^{-2}), uniformly distributed on the faces $F_j^\pm$ of all the discs C_j. Thus denoting by V_{cyt} the volume of the cytosol in the ROS, and denoting by A_{discs} the surface area of all

disc faces,

$$k_{\sigma;hyd}[PDE]_\sigma[cG]A_{discs} = k_{hyd}[PDE][cG]V_{cyt} \qquad (14)$$

The product $k_{hyd}[PDE]$ is denoted by β_{dark} in [1]. For the salamander, $k_{hyd} \simeq 0.05\ \mu M^{-1} s^{-1}$ [14] and $[PDE] \simeq 20\ \mu M$ [15], whence $\beta_{dark} \simeq 1\ s^{-1}$. The volume-to-surface ratio V_{cyt}/A_{discs} for salamander is estimated from the geometry of the ROS and Table 2

$$\eta \overset{\text{def}}{=} \frac{V_{cyt}}{A_{discs}} \simeq \frac{1}{2}\nu\varepsilon = 0.007\ \mu m \qquad (15)$$

With this notation, the flux generated on the faces $F_j^\pm$, owing to hydrolysis of cGMP by dark-activated PDE, is

$$k_{\sigma;hyd}[PDE]_\sigma[cG] = \eta\beta_{dark}[cG] \qquad (16)$$

Production of cGMP is mediated by guanylyl cyclase (GC), which is located on the faces of the discs C_j. Molecules of guanosine triphosphate (GTP) bind to molecules of GC to synthesise cGMP. Such activity is modulated by Ca^{2+}, being maximum for $[Ca] = 0$ and minimum for $[Ca] \to \infty$. The cGMP production rate per unit GC surface density can be described by a Hill-type law

$$k_{\{GC;o\}}[GC]_\sigma \overset{\text{def}}{=} k_{\{GC;\min\}}[GC]_\sigma$$
$$+ \frac{k_{\{GC;\max\}}[GC]_\sigma - k_{\{GC;\min\}}[GC]_\sigma}{1 + ([Ca]/K_{cyc})^{m_{cyc}}}$$

where $k_{\{GC;max\}}$ and $k_{\{GC;min\}}$ are the surface catalytic rates of GC at $[Ca] = 0$ and $[Ca] \to \infty$, respectively, K_{cyc} is a scaling Ca^{2+} concentration for the cyclase effect, and m_{cyc} is the Hill exponent. The flux on the faces $F_j^\pm$ is $\pm k_{\{GC;o\}}[GC]_\sigma$, where $[GC]_\sigma$ is the surface density of GC. To our knowledge, the literature does not contain measurements of the surface catalytic rates $k_{\{GC;max\}}$ and $k_{\{GC;min\}}$, nor of the corresponding volumic rates $k_{\{GC;max;vol\}}$ and $k_{\{GC;min;vol\}}$. It does contain, however, measurements of

$$\alpha_{max} \overset{\text{def}}{=} k_{\{GC;max;vol\}}[GC] \quad \text{and}$$
$$\alpha_{min} = k_{\{GC;min;vol\}}[GC]$$

as if GC were uniformly distributed in the ROS. A conversion argument similar to the one leading to (16) gives the production flux of cGMP across $F_j^\pm$, due to GC, in the form

$$\mp\eta\alpha \quad \text{where } \alpha = \alpha_{min} + \frac{\alpha_{max} - \alpha_{min}}{1 + ([Ca]/K_{cyc})^{m_{cyc}}} \qquad (17)$$

Let C_{j_*} be a disc hit by one or several photons on one of its faces, say for example $F_{j_*}^-$, and let $[PDE^*]_\sigma(\bar{x}, t)$ be the resulting surface density of activated PDE molecules, as a function of space and time. Let also $k^*_{\sigma;hyd}$ denote the surface catalytic rate of light-activated PDE (measured in (number of molecules $\mu m^{-3})^{-1} s^{-1}$). The flux generated on $F_{j_*}^-$ by such a depletion of cGMP is then

$$k^*_{\sigma,hyd}[PDE^*]_\sigma[cG] \qquad (18)$$

The determination of the rate $k^*_{\sigma;hyd}$ will be discussed in Section 2.4.2. The above considerations yield the following boundary condition for $[cG]$ on each of the faces $F_j^\pm, j = 1, \ldots, n$:

$$-D_{cG}\frac{\partial}{\partial z}[cG]\Big|_{F_j^\pm} = \eta(\pm\alpha \mp \beta_{dark}[cG])$$
$$+ \delta_j k^*_{\sigma,hyd}[PDE^*]_\sigma[cG] \qquad (19)$$

where δ_j equals 1 if $j = j_*$ (activated face) and it is zero otherwise. By (15), the factor η is of the order of ε, which is crucial for the homogenisation process.

We finally assume that cGMP does not penetrate the lateral part L_j of the discs C_j, nor does it flow out of the ROS, i.e.

$$D_{cG}\nabla[cG] \cdot \boldsymbol{n}\big|_{L_j} = 0 \qquad D_{cG}\nabla[cG] \cdot \boldsymbol{n}\big|_{\partial\Omega_\varepsilon} = 0 \qquad (20)$$

where $\boldsymbol{n}$ is the unit normal to the indicated surfaces pointing outside the ROS.

Assume n_* discs are activated, each by one or several photons, and each on their lower faces $F_{j_*}^-$; we relabel and order them as C_{j_*} for $j_* = 1, \ldots, n_*$. Then the flux conditions on the faces $F_j^\pm$ are expressed as in (19), where δ_j equals 1 if $j \in \{1, \ldots, n_*\}$, and it is zero otherwise.

2.2.2 Boundary conditions for [Ca]:
$[Ca]$ flows into the cytoplasm through cGMP-gated channels and is extruded by the electrogenic exchanger. Thus the boundary fluxes for $[Ca]$ can be expressed as

$$-D_{Ca}\nabla[Ca] \cdot \boldsymbol{n} = \frac{1}{\Sigma_{rod}B_{Ca}\mathcal{F}}\left(J_{ex} - \frac{1}{2}f_{Ca}J_{cG}\right) \qquad (21)$$

The currents J_{ex} and J_{cG} (measured in pA) were defined in (3) and (4). The constant B_{Ca} is the buffering power of the cytoplasm for $[Ca]$, f_{Ca} is the fraction of cGMP-activated current carried by Ca^{2+}, $\mathcal{F}$ is the Faraday constant, and Σ_{rod} is the lateral surface area of the ROS.

In [1], the currents J_{ex} and J_{cG} contribute with a volumic term to the variation of $[Ca]$, i.e. j_{ex}^{sat} and j_{cG}^{max} are divided by V_{cyt} (1 picolitre). As both currents are generated on the lateral boundary of the ROS and are local in nature, they are taken here as surface current densities and thus as boundary sources for $[Ca]$. Calcium does not penetrate the disc C_j, nor does it flow out of the ROS through its top $\{z = H\}$ or its bottom $\{z = 0\}$. Therefore

$$\nabla[Ca]\big|_{\partial C_j} \cdot \boldsymbol{n}_j = 0 \quad \text{and} \quad \frac{\partial[Ca]}{\partial z} = 0$$
$$\text{for } z = 0 \text{ and } z = H \qquad (22)$$

where $\boldsymbol{n}_j$ is the unit normal to C_j.

In summary, the full three-dimensional space-time model for cGMP and $[Ca]$ consists of the partial differential equations (11), the initial conditions (12) and the boundary conditions (19)–(22).

2.2.3 Activation mechanism:
Light activation is embodied in the term $[PDE^*]_\sigma$ appearing in (19). The literature contains various attempts to describe such a quantity [1, 2, 4, 8, 16–19]. A satisfactory, full modelling of the function $[PDE^*]_\sigma(\bar{x}, t)$ for $\bar{x} = (x_1, x_2)$ ranging over one of the faces of an activated disc C_{j_*} would have to emerge from a careful, pointwise modelling of the cascade receptor $\rightarrow$ transducer $\rightarrow$ effector on the activated discs. Until such a detailed description is achieved, we consider here a lumped activation mechanism proposed by [20]. By such a model, the total number of activated PDEs in the ROS, although changing in time, is instantaneously distributed, equally and uniformly, on the n_* activated faces $F_{j_*}^-$. In this way, the surface density of activated PDE is the total number of PDE* molecules in the ROS divided by the area $\{n_*\pi R^2\}$ of activated faces. Full activation is also assumed, that is PDE* is defined to be activated if both of its γ subunits have been removed. Denote by $E^*(t)$ the number of γ subunits that have been removed from PDE

at time t, in the entire ROS. Then

$$[PDE^*]_\sigma = \frac{number\ of\ molecules\ of\ PDE^*\ in\ ROS}{n_*\pi R^2}$$
$$\overset{\text{def}}{=} \frac{(1/2)E^*(t)}{n_*\pi R^2} \qquad (23)$$

Following [2, 20], the quantity $E^*(t)$ is approximated in terms of two first-order rate constants k_R, k_E, representing decay of R* and concurrent G*-PDE* decay, as

$$E^*(t) = \Phi\left(\frac{v_{RE}}{k_R - k_E}\right)(e^{-k_E t} - e^{-k_R t}) \quad \text{for } t > 0 \qquad (24)$$

where Φ is the number of photo-isomerisations per rod per flash, and v_{RE} is the effective rate with which a single R* triggers activation of PDE*. (According to [20], the activation cascade involves three delay time constants, t_R, t_G and t_E. The quantity $E^*(t)$ in (24) is meant for times larger than the sum of these three delay times, i.e. for $t > t_{RGE} = t_R + t_G + t_E$. Such 'initial time' has been renormalised to be zero.)

The rate constant v_{RE} depends on diffusion coefficients and the probability of successful encounters of R* with G and of G* with PDE. The rates k_R and k_E are interchangeable in (24), and so, with this type of activation, the model cannot distinguish which of the two rate constants is the rate-limiting one.

2.3 Homogenised model

The model is derived by regarding ε as a small parameter to be allowed to go to zero, starting from its initial physical value $\varepsilon_o = 14$ nm. The limit process keeps constant the volume fraction of the ROS available for diffusion. Therefore, as, when $\varepsilon \rightarrow 0$, the discs C_j become thinner, we artificially increase their number in such a way that the volume fraction θ_o in (1) remains constant. The faces $F_{j_*}^-$ where a photon is captured are at levels z_{j_*} for $j_* = 1, 2, \ldots, n_*$. The limit is carried out so that the levels z_{j_*} are kept fixed for all $\varepsilon > 0$.

In the limit, the discs are conceptually removed, and we obtain a limiting ROS, denoted by Ω, which is a cylinder of radius R, height H and lateral boundary S, given by

$$S = \{(\bar{x}, z) \mid |\bar{x}| = R; z \in (0, H)\}$$
$$= \{(R, \theta, z) \mid \theta \in [0, 2\pi), z \in (0, H)\} \qquad (25)$$

The outer shell of the ROS, i.e. the gap $\Omega_\varepsilon - \Omega$, is a thin cylindrical layer of thickness $\sigma\varepsilon$. Likewise, the n_* interdiscal spaces I_{j_*} adjacent to the faces $F_{j_*}^-$, where the photons are captured, are thin cylindrical layers of thickness $v\varepsilon$. As $\varepsilon \rightarrow 0$, they disappear in the limit and provide no limiting information on the diffusion of cGMP and Ca^{2+} within them. In these thin layers, the diffusivity and capacity coefficients in (11) are concentrated (i.e. they are multiplied by ε^{-1}), to compensate for their shrinkage of the same order. The remaining layers are also thin, of the order of ε; however, there are roughly speaking ε^{-1} of them, and so the information in them is compounded in the limit. This way, for $\varepsilon > 0$, the system in (11) is a system of diffusion equations with discontinuous coefficients that become unbounded as $\varepsilon \rightarrow 0$. The boundary conditions (19, 20) for cGMP and (21, 22) for Ca^{2+} remain unchanged. The solutions of such a three-dimensional model with discontinuous and unbounded coefficients are denoted by $[cG]_\varepsilon$ and $[Ca]_\varepsilon$.

IEE Proc.-Syst. Biol., Vol. 152, No. 3, September 2005

123

The rigorous calculation of the limiting problem is presented in [3]. The pointwise interpretation of such a limit is in [4]. Here, we reproduce the limit in its weak formulation, which is the form suitable for numerical calculations.

As $\varepsilon \to 0$, the approximating functions $[cG]_\varepsilon$ and $[Ca]_\varepsilon$ generate three pairs of functions:

• $[cG]$ and $[Ca]$, defined in Ω and called the interior limit. They satisfy a two-dimensional diffusion process (diffusion occurs only along the transverse variables $\bar{x} = (x_1, x_2)$, on each level z and on each disc $D_R = \{|\bar{x}| < R\}$.

• $[cG]_s$ and $[Ca]_s$, defined in S and called limit in the outer shell. They satisfy two-dimensional surface diffusion processes on the limiting outer shell S and they 'glue' together along S the diffusion processes of the indicated interior limit.

• $[cG]_*$ and $[Ca]_*$, defined on the discs $\mathcal{D}_R \times \{z_{j_*}\}$, for $j_* = 1, 2, \ldots, n_*$, and called limit at the activation sites. They satisfy diffusion processes that directly respond to activation and transmit the signal to the rest of the ROS.

These functions are smooth and satisfy the usual compatibility conditions; for example, the interior limit $[cG]$ computed on S equals $[cG]_s$. However, $[cG]$ computed for $z = z_{j_*}$ is not $[cG]_*$.

The indicated diffusion processes can be written down as a system of two partial differential equations, one for $[cG]$ and one for $[Ca]$. These equations have been derived in [3], and their biophysical significance is discussed in [4]. The formulations below, (26) for $[cG]$ and (27) for $[Ca]$, are equivalent to the indicated systems of partial differential equations and are reported in this form as they are the starting point of the numerical simulations.

Let α be defined as in (17) for $[Ca]$ equal to the interior limit of $[Ca]_\varepsilon$. Define also α_* as in (17), with $[Ca]$ replaced by $[Ca]_*$ and set

$$P = \beta_{dark}[cG] - \alpha$$

$$P_{j_*} = \left(\beta_{dark}[cG]_* - \alpha_* + \frac{1}{v\varepsilon_o} k^*_{\sigma;hyd}[PDE^*]_\sigma[cG]_* \right)\bigg|_{z=z_{j_*}}$$

Let also J_{ex} and J_{cG} be the currents in (3) and (4), with $[Ca]$ and $[cG]$ replaced by $[Ca]_s$ and $[cG]_s$. Then set

$$Q = \frac{1}{\sigma\varepsilon_o} \frac{1}{\Sigma_{rod} B_{Ca} \mathcal{F}} \left(J_{ex} - \frac{1}{2} f_{Ca} J_{cG} \right)$$

With this notation, the weak formulation of the homogenised limiting problem for cGMP takes the form

$$0 = (1 - \theta_o) \int_0^\tau \int_\Omega \left\{ \frac{\partial}{\partial t}[cG]\varphi + D_{cG}\nabla_{\bar{x}}[cG] \right.$$

$$\left. \cdot \nabla_{\bar{x}}\varphi + P\varphi \right\} d\Omega\, dt + \sigma\varepsilon_o \int_0^\tau \int_S \left\{ \frac{\partial}{\partial t}[cG]_s\varphi \right.$$

$$\left. + D_{cG}\nabla_S[cG]_s \cdot \nabla_S\varphi \right\} dS\, dt$$

$$+ v\varepsilon_o \sum_{j_*=1}^{n_*} \int_0^\tau \int_{\mathcal{D}_R} \left\{ \frac{\partial}{\partial t}[cG]_*\varphi \right.$$

$$\left. + D_{cG}\nabla_{\bar{x}}[cG]_* \cdot \nabla_{\bar{x}}\varphi + P_{j_*}\varphi \right\} d\mathcal{D}_R\, dt \qquad (26)$$

Here, $\tau > 0$ is an arbitrary time value, $\nabla_{\bar{x}}$ is the gradient with respect to the transverse variables $\bar{x} = (x_1, x_2)$ only, ∇_S is the gradient on the surface S, and $d\Omega$, dS, $d\mathcal{D}_R$ are

the volume or surface measures on Ω, S and $\mathcal{D}_R$, respectively. The testing function φ (and ψ below) is arbitrary and smooth up to the boundary of Ω. The limiting weak formulation for Ca^{2+} is, with similar notation,

$$0 = (1 - \theta_o) \int_0^\tau \int_\Omega \left\{ \frac{\partial}{\partial t}[Ca]\psi + D_{Ca}\nabla_{\bar{x}}[Ca] \cdot \nabla_{\bar{x}}\psi \right\} d\Omega\, dt$$

$$+ \sigma\varepsilon_o \int_0^\tau \int_S \left\{ \frac{\partial}{\partial t}[Ca]_s\psi + D_{Ca}\nabla_S[Ca]_s \right.$$

$$\left. \cdot \nabla_S\psi + Q\psi \right\} dS\, dt + v\varepsilon_o \sum_{j_*=1}^{n_*} \int_0^\tau \int_{\mathcal{D}_R \times \{z_{j_*}\}}$$

$$\left\{ \frac{\partial}{\partial t}[Ca]_*\psi + D_{Ca}\nabla_{\bar{x}}[Ca]_* \cdot \nabla_{\bar{x}}\psi \right\} d\mathcal{D}_R\, dt \qquad (27)$$

As indicated earlier, the geometry becomes simple, but the mathematical form of the homogenised limit bears no intuitive connection with the physics of the phenomenon and calls for a numerical verification of such a model. In the following sections, we will present a series of numerical experiments that indicate that the homogenised limit is faster to compute and yields a relative response close to that of the full three-dimensional model, with an accuracy of at least 0.03% (Fig. 3).

2.4 Parameters

The definitions of the variables and parameters are listed in Table 1. The values of parameters used in the simulations are listed in Table 2, along with their sources.

All the parameter values used in this work are for the ROS of salamander. Parameter values were chosen to be consistent with previous modelling studies in salamander, so that the results would be comparable.

2.4.1 Diffusion coefficients: The effective longitudinal diffusion coefficient $D_{cG;eff}$ of cGMP, which is measured in experiments [16, 21, 13] can be related to the cytoplasmic diffusion coefficient D_{cG} by the formula [4, 7, 13]

$$D_{cG;eff} = (f_A/f_V)D_{cG} \qquad (28)$$

where the ratio (f_A/f_V) of the effective cross-sectional area to the effective volume available for longitudinal diffusion is a geometric factor giving a measure of tortuosity, i.e. the physical hindrance to longitudinal diffusion arising from the disc stack. From electron micrographs of salamander disc cross-sections, [13] estimated $f_A \simeq 0.014$ and $f_V \simeq 0.5$, so that $f_A/f_V \simeq 0.028$, and deduced that the effective longitudinal coefficient $D_{cG;eff}$ is 1.4–$5.5\ \mu m^2\ s^{-1}$. Hence, the diffusion coefficient for cGMP is estimated to be in the range

$$D_{cG} = (f_V/f_A)D_{cG;eff} \simeq 50\text{–}196\ \mu m^2\ s^{-1} \qquad (29)$$

Koutalos *et al.* [16] estimated $D_{cG;eff} \simeq 30$–$60\ \mu m^2\ s^{-1}$. They also argued that preparation of the ROS for microscopy could decrease the hindrance constant (f_A/f_V) and suggested $(f_A/f_V) \simeq 0.04$. For these values, (28) would imply that D_{cG} is in the range 750–$1500\ \mu m^2\ s^{-1}$. Even neglecting viscosity and buffering effects, the latter seems to be considerably higher than the common estimate of the aqueous diffusion coefficient of cGMP ($\simeq 500\ \mu m^2\ s^{-1}$). In [9], the value $D_{cG;eff} \simeq 18.5\ \mu m^2\ s^{-1}$ is reported, which, for $(f_A/f_V) \simeq 0.028$ and no buffering nor viscosity effects, corresponds to $D_{cG} \simeq 660\ \mu m^2\ s^{-1}$ and, for $(f_A/f_V) \simeq 0.04$, corresponds to $D_{cG} \simeq 460\ \mu m^2\ s^{-1}$.

Table 1: Nomenclature

Symbol	Units	Definition	Reference
α, α_{min}, α_{max}	$\mu M\,s^{-1}$	rate of synthesis of cGMP by guanylyl cyclase	[17], Section 2.2.1
A_{discs}	μm^2	surface area of disc faces; of activated faces	[15], Sections 2.2.1, 2.2.2
β_{dark}	s^{-1}	rate of cGMP hydrolysis by PDE	[16], Sections 2.2.1, 2.3, 2.4.2
B_{Ca}; B_{cG}	—	buffering power of cytoplasm for Ca^{2+}; cGMP	[21], Section 2.2.2, [35], Section 2.4.3
$[Ca]$; $[cG]$	μM	concentration of calcium ions; of cGMP	[11], Section 2.2
D_{Ca}; D_{cG}	$\mu m^2\,s^{-1}$	diffusion coefficient for Ca; cGMP	[11], Section 2.2
ε; $\nu\varepsilon$	μm	disc thickness; interdiscal space	Section 2.1.1
E^*	subunits	number of activated PDE subunits per ROS	[23, 24], Section 2.2.3
f_{Ca}	—	fraction of cGMP-activated current carried by Ca^{2+}	[21], Section 2.2.2
$\mathcal{F}$	$C\,mol^{-1}$	Faraday's constant	[21], Section 2.2.2
Φ	isom.	intensity of brief flash	[24], Section 2.2.3
η	μm	volume-to-surface ratio: V_{cyt}/A_{discs}	[15], Section 2.2.1
H	μm	height of ROS	Section 2.1.1
J	pA	total circulating current ($J = J_{ex} + J_{cG}$)	[7], Section 2.1.3
J_{dark}	pA	dark current	Sections 2.1.3, 2.4.3
$J_{dark} - J$	pA	response	Section 2.1.3
$1 - J/J_{dark}$	pA	relative response	Section 2.1.3
j_{ex}^{sat}	pA	saturation exchange current	[3], Section 2.1.3
j_{cG}^{max}	pA	maximum exchange current	[4], Section 2.1.3
k_{cat}/K_m	$\mu M^{-1}s^{-1}$	hydrolytic efficacy of activated PDE dimer	[37], Section 2.4.3
k_E	s^{-1}	rate constant for inactivation of PDE*	[24], Section 2.2.3
k_R	s^{-1}	rate constant for inactivation of Rh*	[24], Section 2.2.3
k_{hyd}	$\mu M^{-1}s^{-1}$	volumetric hydrolysis rate of cGMP by PDE	[14], Sections 2.2.1, 2.4.3
$k_{\sigma;hyd}$	$\mu m^3 s^{-1}$	surface hydrolysis rate of cGMP by PDE	[13], Sections 2.2.1, 2.4.3
$k_{\sigma;hyd}^*$	$\mu m^3 s^{-1}$	surface hydrolysis rate of cGMP by PDE*	[18], Sections 2.2.1, 2.4.3
K_{cyc}	μM	half maximum constant for cyclase effect	[17], Section 2.2.1
K_{cG}	μM	cGMP concentration for half maximum channel opening	[4], Section 2.1.3
K_{ex}	μM	Ca^{2+} concentration for half maximum channel opening	[3], Section 2.1.3
m_{cG}; m_{cyc}	—	Hill exponents	[4, 17], Sections 2.1.3, 2.2.1
v_{RE}	s^{-1}	rate of E* formation per fully activated Rh*	[24], Sections 2.2.3, 2.4.3
n; n_*	—	number of discs; of activated discs	Sections 2.2.1, 2.3
N_{Av}	mol^{-1}	Avogadro number	Section 2.4.3
$[PDE]_\sigma$	number of molecules μm^{-2}	surface density of dark-activated PDE	[14], Section 2.2.1
$[PDE^*]_\sigma$	number of molecules μm^{-2}	surface density of light-activated PDE*	[18], Sections 2.2.1, 2.4.3
R	μm	radius of discs	Section 2.1.1
R_{rod}	μm	$= R + \sigma\varepsilon_o$ = radius of ROS	Section 2.1.1
Rh^*	number of molecules	number of activated rhodopsins in ROS	Section 2.1.2
Σ_{rod}	μm^2	lateral surface area of ROS	[7], Section 2.1.1
V_{cyt}	μm^3	volume of cytosol in ROS	[18], Section 2.2.1
$\tilde{\Omega}_\varepsilon$	—	domain occupied by cytosol in ROS	Section 2.1.1

isom. denotes number of photoisomerisations; — signifies dimensionless quantity

We have not found an attempt to reconcile these seemingly different ranges, nor alternative measurements of D_{cG}.

In the simulations, we use $D_{cG} = 100\ \mu m^2\,s^{-1}$, with $v_{RE} = 195$ (see Section 2.4.4).

The diffusion coefficient of $[Ca]$ in cytosol, $D_{Ca} = 15\ \mu m^2\,s^{-1}$, is taken from [22]. This value accounts for buffering effects on $[Ca]$.

2.4.2 Dark steady state: It is assumed that, in the absence of light, the system is in a uniform steady state $[cG] = [cG]_{dark}$ and $[Ca] = [Ca]_{dark}$ (in μM), and our initial condition is this dark equilibrium state. Accordingly, $[cG]_{dark}$ and $[Ca]_{dark}$ are computed as those values for which all boundary fluxes in (19) and (21) are zero. This yields the equations

$$\left(\alpha_{min} + \frac{\alpha_{max} - \alpha_{min}}{1 + ([Ca]_{dark}/K_{cyc})^{m_{cyc}}}\right) = \beta_{dark}[cG]_{dark} \quad (30)$$

$$\frac{j_{ex}^{sat}}{1 + K_{ex}/[Ca]_{dark}} = \frac{1}{2}\,f_{ca}\,\frac{j_{cG}^{max}}{1 + (K_{cG}/[cG]_{dark})^{m_{cG}}} \quad (31)$$

Substituting $[cG]_{dark}$ from the first into the second yields

$$(\beta_{dark}K_{cG})^{m_{cG}}\left(\alpha_{min} + \frac{\alpha_{max} - \alpha_{min}}{1 + ([Ca]_{dark}/K_{cyc})^{m_{cyc}}}\right)^{-m_{cG}}$$
$$= \frac{1}{2}\,f_{Ca}\,\frac{j_{cG}^{max}}{j_{ex}^{sat}}\left(1 + \frac{K_{ex}}{[Ca]_{dark}}\right) - 1 \quad (32)$$

This is solved for $[Ca]_{dark}$ (e.g. by the bisection method), and then the value of $[cG]_{dark}$ is computed from the first. A necessary condition for (32) to admit a positive solution is

$$\left(\frac{\beta_{dark}K_{cG}}{\alpha_{min}}\right)^{m_{cG}} > \frac{1}{2}\,f_{Ca}\,\frac{j_{cG}^{max}}{j_{ex}^{sat}} - 1 \quad (33)$$

With the values from Table 2, we find that such a restriction is satisfied for $\alpha_{min} < 5.5\ \mu M\,s^{-1}$. This contains the range of literature values. With parameter values from Nikonov *et al.* [1], we find $[cG]_{dark} = 2.91\ \mu M$ and $[Ca]_{dark} = 0.60\ \mu M$. This is slightly less than the dark values of 3 and 0.64 appearing in Nikonov *et al.* [1]. By taking $K_{cyc} = 0.135\ \mu M$, which is also within the published

Table 2: Parameters of the model (for salamander ROS)

Symbol	Units	Range of values	Used in simulation	Reference
α_{max}	$\mu M\,s^{-1}$	40–50	50	[1, 2]
$\alpha_{min}/\alpha_{max}$	—	0.0–0.02	0.02	[1, 2]
β_{dark}	s^{-1}	1	1	[1, 2]
B_{Ca}	—	10–50	20	[1, 2, 20]
B_{cG}	—	1–2	1	[1, 2]
$[cG]_{dark}$	μM	2–4	3	[1, 23]
$[Ca]_{dark}$	μM	0.4–0.7	0.65	[1, 23]
D_{Ca}	$\mu m^2\,s^{-1}$	15	15	[22]
D_{cG}	$\mu m^2\,s^{-1}$	50–196	100	[13, 16]
$\varepsilon_o;\,\nu\varepsilon_o$	μm	0.01–0.014	0.014	[2, 23]
f_{Ca}	—	0.1–0.2	0.17	[1, 2]
$\mathcal{F}$	$\mathcal{C}\,mol^{-1}$	96 500	96 500	[1, 2]
η	μm	—	$\simeq 0.007$	Section 2.2.1
H	μm	20–28	22.4	[2, 23]
J_{dark}	pA	(computed)	66	Section 2.4.2
j_{ex}^{sat}	pA	17–20	17	[2]
j_{cG}^{max}	pA	70–7000	7000	[1]
k_{cat}/K_m	$\mu M^{-1}\,s^{-1}$	340–600	600	[1, 24]
k_E	s^{-1}	0.58–0.76	0.67	[20]
k_R	s^{-1}	1.69–3.48	2.56	[20]
$k_{\sigma;hyd}$	$\mu m^3\,s^{-1}$	—	7×10^{-5}	Sections 2.2.1, 2.4.3
$k_{\sigma;hyd}^*$	$\mu m^3\,s^{-1}$	—	1	Section 2.4.3
K_{cyc}	μM	0.10–0.23	0.135	[1, 23]
K_{cG}	μM	13–32	32	[1, 23]
K_{ex}	μM	1.5, 1.6	1.5	[1, 23]
m_{cG}	—	2	2	[2]
m_{cyc}	—	2–3	2	[1, 16]
v_{RE}	s^{-1}	120, 150, 220	195	[1, 2]; Sections 2.2.3, 2.4.4
n	—	~ 1000	800	[1, 23]
$[PDE]_\sigma$	μm^{-2}	100	100	[2]
R	μm	5.5	5.5	[2, 23]
$R_{rod} = R + \sigma\varepsilon_o$	μm	5.515	5.515	[2, 23]
$\sigma\varepsilon_o$	μm	0.015	0.015	[2, 23]
Σ_{rod}	μm^2	—	776	[23]
V_{cyt}	μm^3	1000	1076	[23]

range 0.10–0.23, we find the more agreeable dark values of 3 and 0.66. Then, from (5, 6), the resulting dark current is $J_{dark} = 66$ pA.

The root of (32) depends most sensitively on β_{dark} and K_{cyc}, then on m_{cyc} and m_{cG}.

2.4.3 Surface catalytic rate: The value of the surface hydrolysis rate $k_{\sigma;hyd}$ is obtained from (15, 16). With $\beta_{dark} \simeq 1\,s^{-1}$ and $[PDE]_\sigma \simeq 100\,\mu m^{-2}$ [2], we find

$$k_{\sigma;hyd} = \frac{\eta\beta_{dark}}{[PDE]_\sigma} \simeq 7 \times 10^{-5}\,\mu m^3\,s^{-1} \qquad (34)$$

To compute $k_{\sigma;hyd}^*$, it is assumed that the same cGMP (in μM) is depleted by a uniform, *volumic* $[PDE^*]$ (in μM), by Michaelis–Menten dynamics, as by a *surface* $[PDE^*]_\sigma$ (in numbers of molecules μm^{-2}), uniformly distributed on the n_* activated faces $F_{j_*}^-$, by surface/volume mass action. Thus, by a conversion argument similar to the one leading to (14),

$$k_{\sigma;hyd}^*[PDE^*]_\sigma[cG] = \frac{k_{cat}}{B_{cG}}\frac{[cG]}{K_m + [cG]}[PDE^*]\frac{V_{cyt}}{n_*\pi R^2} \quad (35)$$

where B_{cG} is the cytoplasmic buffering power of cGMP, K_m is the Michaelis constant, and k_{cat} is the *volumic* catalytic rate of hydrolysis of cGMP. Translating the concentration $[PDE^*]$ to number of subunits E^* using $[PDE^*]N_{Av}V_{cyt} = 1/2E^*$, with N_{Av} the Avogadro number,

taking into account (23) and cancelling out $[cG]$, we find

$$k_{\sigma;hyd}^*[PDE^*]_\sigma = \frac{1}{N_{Av}B_{cG}}\frac{k_{cat}}{K_m + [cG]}[PDE^*]_\sigma \qquad (36)$$

Earlier measurements of the Michaelis constant estimated $K_m \geq 40\,\mu M$. Therefore, as $[cG] \leq 4\,\mu M$, it was common to approximate [23]

$$\frac{k_{cat}}{K_m + [cG]} \simeq \frac{k_{cat}}{K_m} \qquad (37)$$

Recent biochemical investigations of [24] measure $K_m \simeq 10\,\mu M$ and render such an approximation less justified. These measurements also yield the range

$$\frac{k_{cat}}{K_m} \simeq 340\text{--}600\,\mu M^{-1}\,s^{-1} \qquad (38)$$

Earlier estimates had this ratio $\simeq 60\,\mu M^{-1}\,s^{-1}$ [14]. To be consistent with other modelling approaches in the literature, we will keep the approximation (37) and adopt the upper value in (38).

Release of cGMP from non-catalytic sites of PDE provides a pool of cGMP that aids recovery. The buffer constant $B_{cG} > 1$ is meant to account for such an effect, as a slowing-down factor of depletion of cGMP due to PDE*. It is uncertain how to account for such an effect and its relevance. It is argued to be significant by some investigators ([23], p. 757) and too slow in time significantly to contribute [25]. It is neglected (e.g. taken to be 1) in [8, 14] and in [24] (p. 535, formula 5). Taking
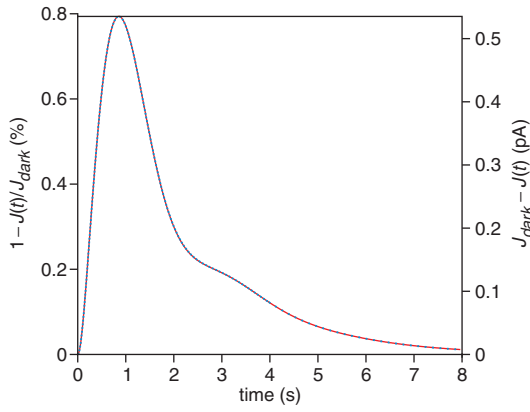
126

IEE Proc.-Syst. Biol., Vol. 152, No. 3, September 2005

Fig. 2 *Single photon response from full and homogenised models*

—— Full model
– – – Homogenised model

Normalised response $(1 - J/J_{dark})$ and response $(J_{dark} - J)$ against time. Peak amplitude of response is 0.54 pA, which amounts to 0.82% suppression in dark standing current of 66 pA. Peak occurs 860 ms after activation. Maximum relative difference between red and blue curves is less than 0.03%

$B_{cG} = 1$ and $k_{cat}/K_m = 600$, we find

$$k_{\sigma;hyd}^* = \frac{600}{N_{Av}} \frac{1}{\mu M} \frac{1}{s} \simeq 1\ \mu m^3\ s^{-1} \qquad (39)$$

We note that the value of $k_{\sigma;hyd}^*$ needs to be about 1 for the simulations to match the experimental data shown in Fig. 5. With $B_{cG} = 2$, the response would be too low unless v_{RE} were taken to be over 500 s^{-1}.

2.4.4 Activation rates:
The values of the rate constants k_R and k_E are reported in Table 2, along with their sources. The values we use in the simulations are within the published ranges.

The parameter v_{RE} represents the activation rate of PDE* per R*. It depends on the probability of successful encounters of Rh* with G and of G* with PDE and thus on many factors that are highly variable and difficult to determine. In disrupted toad ROS experiments, [24] estimated $v_{RE} \sim 120$ s^{-1}. In [2] it is taken to be 150, and in [1] it is taken to be 220 s^{-1}. Earlier values were an order of magnitude higher, e.g. 3500 s^{-1} in [26], and 1000 s^{-1} in [19].
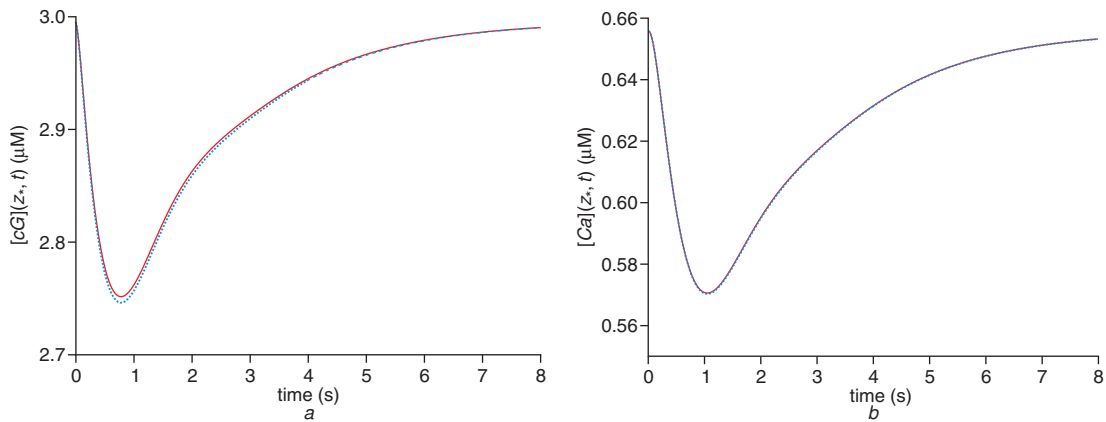
In (24), v_{RE} regulates the initial slope and thus the achievable peak response. Once all other parameters are chosen, v_{RE} can be adjusted to produce a desired peak response. In extensive simulations, we found that the value of v_{RE} necessary to match the 0.8% peak of the experimental data (Fig. 5) depends strongly on the values used for D_{cG} and $k_{\sigma;hyd}^*$. With $D_{cG} = 100\ \mu m^2\ s^{-1}$ and $k_{\sigma;hyd}^* = 1\ \mu m^3\ s^{-1}$, in the simulations we use $v_{RE} = 195$ s^{-1}.

3 Results

3.1 Comparison of full and homogenised models

Figures 2–4 display simulations of the single-photon response in an 800-disc salamander rod photoreceptor by both the full and the homogenised models. The 400th disc is activated (at its lower face) by a single photon, by the activation mechanism of Section 2.2.3, with parameters from Table 2.

In the full model, the rather fine mesh described in Appendix 2 was used (34 radial by $4 \times 800 = 3200$ axial nodes); the entire 8 s simulation (on four networked Intel Xeon 3 GHz workstations) took about 108 h total, equivalent to ~430 CPU h on a single processor.

As mentioned in Appendix 3, we tried various mesh sizes with the homogenised model and found that 16 radial and 120 axial nodes give excellent agreement with the full model, as can be seen in Figs. 2–4. The 8 s simulation took only 300 s (on an Intel Xeon 3 GHz), which amounts to a spectacular speedup by a factor of ~5200 compared with the full model.

3.2 Single-photon response

Several additional results for the single-photon response of the salamander rod photoreceptor are shown in Figs. 6–9. Again, the full and homogenised models produce essentially identical results, except for Fig. 9, showing radial profiles of cGMP just above the activated disc; the homogenised model cannot distinguish the upper and lower faces of the activated disc, and so it produces r-profiles symmetric with respect to the activated disc.

The simulations show that a single photoisomerisation has considerable *local* effect (near the activation site) on both transverse and longitudinal diffusion of the second messengers cGMP and Ca^{2+} and thus also on current.
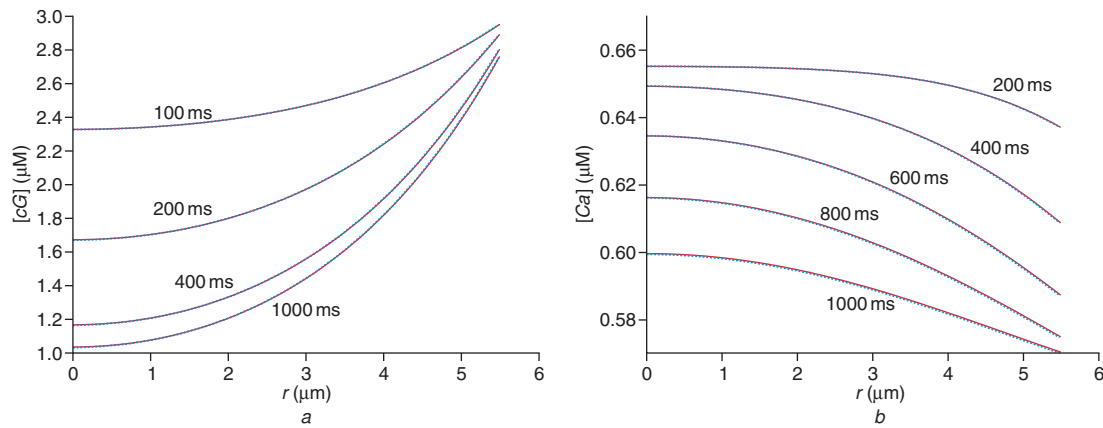

Fig. 3 *Concentration histories from the full and homogenised models, at lateral membrane at activation level z_**

—— Full model
– – – Homogenised model

Initial concentrations $[cG]_{dark}$ and $[Ca]_{dark}$ are, respectively, 3 and 0.66 μM. (*a*) $[cG](z_*, t)$ against time; maximum depletion 7.91% at time 790 ms. (*b*) $[Ca](z_*, t)$ against time; maximum depletion 12.84% at time 1060 ms. Maximum relative difference between red and blue curves: *a* 0.19% and *b* 0.05%

Fig. 4 *Concentration radial profiles just below activated disc from full and homogenised models*

—— Full model
– – – Homogenised model
(*a*) Radial profiles of $[cG](r, z_*, t)$ at times 200, 400, 1000 ms. (*b*) Radial profiles of $[Ca](r, z_*, t)$ every 200 ms. *r*-profiles of $[Ca](r, z, t)$ above and below activated disc are very similar, whereas those of $[cG](r, z, t)$ are not (compare *a* with Fig. 9). Maximum relative difference between red and blue curves is 0.37% for cGMP and 0.07% for Ca^{2+}

In Fig. 5, we superimpose the simulated normalised response of Fig. 2 (thick red curve) on experimental measurements of the single photon response of salamander ROS. The simulation captures well the peak response, the time at which it occurs and the tail of the recovery, but it displays a steeper recovery than the data. One possibility for the less satisfactory agreement in the recovery phase may be that the calcium feedback needs improvement. Another reason may be due to the basic activation mechanism (Section 2.2.3) employed in the simulation. Future refinements of the model will improve upon this mechanism.

Various aspects of the behaviour of the rod photoreceptor, seen in Figs. 2–9, are summarised and further discussed below.

The peak amplitude of the response, $J_{dark} - J$, is about 0.54 pA, with $J_{dark} = 66$ pA, which amounts to 0.82% suppression in the dark standing current; it occurs at time 860 ms after light activation. However, the local response at the activated disc is much greater ($\sim$15%, Fig. 6).
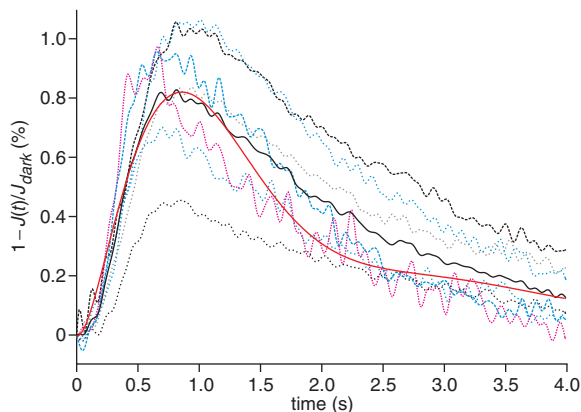
The suppression of dark current results from highly localised depletion of $[cG]$ and $[Ca]$ (Fig. 8) about the activated 400th disc at the plasma membrane. The peak depletion of $[cG](z_*, t)$ is 8% at time 800 ms, whereas $[Ca](z_*, t)$ decreases more, $\sim$13%, and later, at 1100 ms.

The response is highly localised about the activated disc, as revealed by the longitudinal profiles of normalised local response $1 - J(z, t)/J_{dark}$ in Figs. 7 and 8. The maximum spread, about z_*, is $\sim$311 discs at time 1300 ms; this amounts to a spread of 8.7 μm, or 39% of the 22.4 μm ROS length. Representative values of spread are listed in Table 3. During recovery, the spread continually recedes to zero. Spread results reported in the literature for other species are discussed in Section 4.4.

The shapes of the *z*-profiles of $[cG](z, t)$ are almost identical to those of current, whereas the *z*-profiles of $[Ca](z, t)$ are more rounded, see Fig. 8*b*. $[cG](z, t)$ spreads up to 282 discs ($\sim$7.9 μm, i.e. $\sim$35% of the ROS length) at time 1200 ms. $[Ca](z, t)$ spreads more, up to 318 discs

Fig. 5 *Comparison of single photon simulation (thick red curve, same as Fig. 2) with seven measured responses in salamander (data of F. Rieke)*

Single photon responses were estimated from suction electrode recordings of average response to 50–100 flashes producing $\sim$2–4 absorbed photons. Responses were divided by mean number of absorbed photons to estimate single photon response. Each cell's data were normalised by its dark current (average 44 pA) to produce the cell's relative response $1 - J/J_{dark}$
The thick black line is their average, salient features of which (peak amplitude and time-to-peak) are captured well by simulation
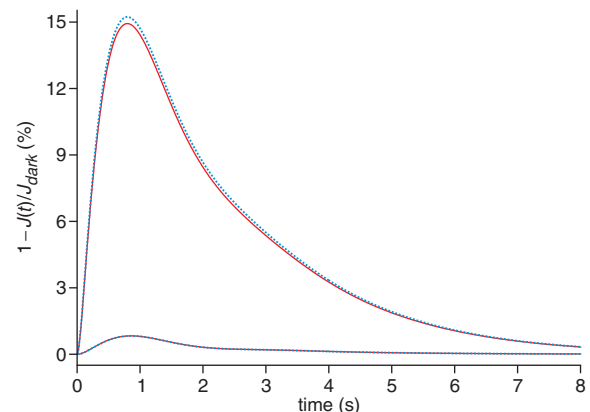

Fig. 6 *Local response at activated 400th disc unit only, normalised by J_{dark}, i.e. $1 - J(z_*, t)/J_{dark}$ and normalised response of entire ROS (same curve as in Fig. 2, reshown here for comparison)*

Upper curve: local response
Lower curve: normalised response
Maximum relative reduction in local current (across plasma membrane corresponding to activated disc unit) is 14.8% (occurring at time 800 ms), whereas, in total current is only 0.82% (at time 860 ms). Thus local response, at activated disc, is $\sim$18 times greater than total (integrated) response. Maximum relative difference between red (full model) and blue (homogenised) curves for local response is 2.00%, whereas for total response it is only 0.03%
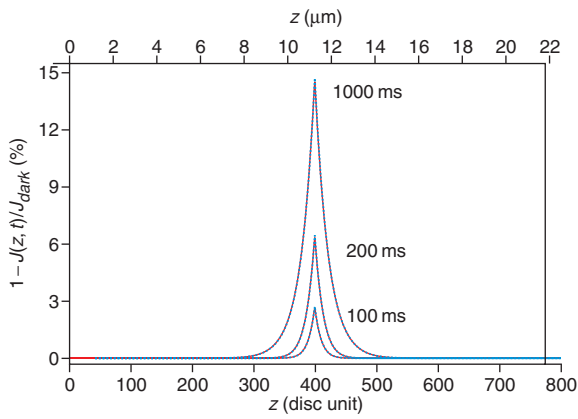
128

IEE Proc.-Syst. Biol., Vol. 152, No. 3, September 2005

Fig. 7 *z-profile of local relative response $1 - J(z, t)/J_{dark}$ at three times, showing highly localised nature of response*

Maximum spread of the response is 311 disc units, occurring at 1300 ms, which amounts to $\lambda_o = 8.7\ \mu m$. Notion of spread is that introduced in (9) of Section 2.1.4. Maximum space constant is $\lambda_* = 0.6\ \mu m$, occurring at 800 ms. Maximum relative difference between red (full model) and blue (homogenised) curves: 2.07% at 100 ms, 1.73% at 200 ms, and 1.25% at 1000 ms

($\sim 8.9\ \mu m$, i.e. $\sim 40\%$ of the ROS length), and later, at time 1500 ms.

The variation, in the radial direction, of the concentrations $[cG](r, z_*, t)$ and $[Ca](r, z_*, t)$ at the activation level z_* is shown in Figs. 4 and 9. During activation, the radial profiles of $[cG]$ become steeper with time, indicating that radial diffusion (especially below the activated disc) might not be negligible, contrary to what has been assumed in several studies [2, 7, 8, 21, 24]. As recovery proceeds, the radial profiles seem to regress and flatten out.

The radial profiles of $[cG](r, z_*, t)$ in the cytosol just above (Fig. 4a) and just below (Fig. 9) the activated disc are quite different in shape, whereas those of $[Ca](r, z_*, t)$ are very similar to each other (Fig. 4b). This is expected from the fact that cGMP is assumed to be hydrolysed by PDE* only on the lower surface of the activated disc, whereas Ca^{2+} is not affected by the discs.

Activating any single disc farther away than about 25 discs from the ends of the ROS produces the same behaviour, with the peak translated at the activation site.

A thinner rod, with 30% smaller disc radius ($R = 3.85\ \mu m$), produces $\sim 50\%$ higher peak response (0.83 pA

or 1.2%, at 750 ms). On the other hand, a wider rod, with 30% larger radius ($R = 7.15\ \mu m$), produces $\sim 30\%$ lower peak response (0.38 pA or 0.58%, at 970 ms). Note that the steady-state dark values are independent of the radius (see (32)), assuming parameters such as β_{dark} remain the same.

3.3 Clamped calcium

Next, we present simulations of single-photon responses when the $[Ca]$ concentration is held fixed at four different values: $[Ca]_{dark} = 0.4, 0.66, 0.8, 1.0\ \mu M$. The corresponding dark values of $[cG]$ that ensure steady state are: $[cG]_{dark} = 6.1, 3.0, 2.4, 1.9\ \mu M$, computed from (30). The corresponding dark currents are: $J_{dark} = 247, 66, 44.5, 31$ pA.

The results are plotted in Fig. 10 and summarised in Table 4. The case of $[Ca]_{dark} = 0.66\ \mu M$ is directly comparable with the normal single-photon response of Fig. 2. The peak response is much higher and occurs much later, and recovery is much slower than the normal unclamped case, as is also observed in various experimental studies [1]. The spread interval exceeds 420 discs (11.8 μm) at 1800 ms, and $\lambda_* = 0.92\ \mu m$. We note that, in Fig. 10, the area under the clamped ($Ca = 0.66$) curve is four times greater than the area under the non-clamped response, similar to measured area ratios [17].

3.4 Multi-photon response

Simulations with a higher intensity stimulus of $\Phi = 7$ photoisomerisations are presented in Fig. 11 and summarised in Table 5. When several discs are activated, we observe that the spacing of activated sites significantly affects the response. Activating discs far apart from each other produces considerably higher response than activating discs adjacent to each other.

In the multiphoton simulations, $\Phi = 7$ photoisomerisations are applied in three different configurations. In one configuration (Figs. 11a and b), the seven photons are applied on one disc (number 400), which produces 2.1% peak response. In the second configuration (Figs. 11c and d), seven adjacent discs (discs number 397–403) are activated with one photon each, resulting in 3.5% peak response. In the third configuration (Figs. 11e and f), seven discs, 100 disc units apart from each other, are
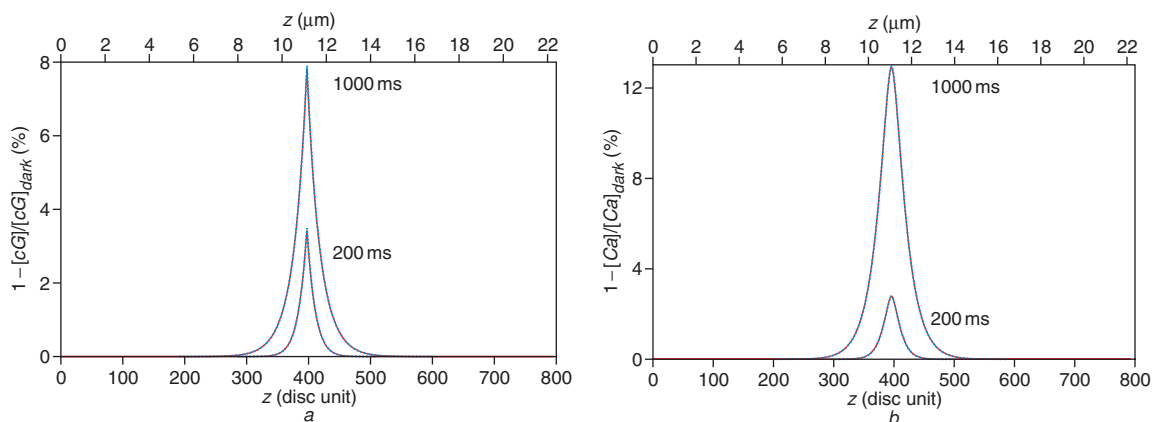

Fig. 8 *z-profiles, about z_*, of depletion of relative local concentrations of $[cG](z, t)$ and $[Ca](z, t)$ at two times*

Normalising factors are $[cG]_{dark} = 3\ \mu M$ and $[Ca]_{dark} = 0.66\ \mu M$
a Depletion $1 - [cG](z, t)/[cG]_{dark}$ against location z; maximum spread is 282 disc units ($\sim 7.9\ \mu m$), occurring at ~ 1200 ms
b Depletion $1 - [Ca](z, t)/[Ca]_{dark}$ against location z; maximum spread is 318 disc units ($\sim 8.9\ \mu m$), occurring at ~ 1500 ms. Maximum relative difference between red (full model) and blue (homogenised) curves: 1.53% at 200 ms, 1.36% at 1000 ms in a, and 0.51% at 200 ms, 0.28% at 1000 ms in b. Notice that $[Ca]$ profiles are more rounded at their peak
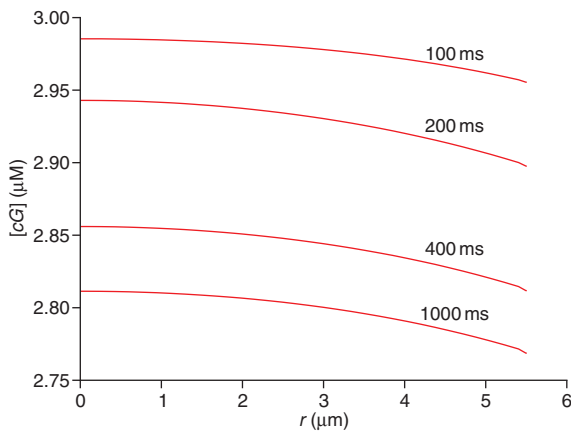
IEE Proc.-Syst. Biol., Vol. 152, No. 3, September 2005

129

Fig. 9 *Radial profiles of [cG](r, z, t) just above activated disc at various times*

Compare with Fig. 4a. Drastically different behaviour of cGMP above and below activated disc is due to its hydrolysis by PDE* on lower face of disc only (see Section 3.2)

activated (discs number 100, 200, 300, 400, 500, 600, 700), which produces a higher peak response of 5.7%.

We note that, in the third case, the local response at each of the activated discs (see Table 5) is almost identical to that of the single-photon case, as might be expected, as the discs hardly interact, and their contributions to the total response are additive. Thus maximum separation produces maximum total response. This phenomenon can create variability of responses to non-saturating light, apart from any other factors, merely according to where (how far apart) photons happen to be absorbed.

For higher Φ, the effect can be much more pronounced than that seen in Fig. 11. For example, as shown in Fig. 12, whereas 700 photons all on one disc produce 4% peak response, they produce 38% peak when distributed on 12 discs lying 70 discs apart from each other, and 86% peak when spread one each on 700 consecutive discs. Considering the enormous number of possible ways that 700 photons could be distributed among 800 discs (in the order of 10^{25}), it is clear that this photon-distribution effect alone can generate tremendous variability in response, essentially any response in the range between minimum and maximum (e.g. between 4% and $\sim$90% for $\Phi = 700$). Minimum response is produced when all the photons are on one disc (adaptation takes over, reducing the response), and maximum response is produced when they are maximally separated, with as few as possible on each disc (to minimise adaptation).

Another way of viewing the phenomenon is that of additivity of individual responses. In experiments, non-linear summation of single-photon responses (SPRs) becomes noticeable (about 10% deviation from linearity) for flashes that suppress 20–25% of the dark current. Our simulations show that non-linear summation occurs at much lower light and it is strictly due to how many discs apart are the discs upon which the photons act. Proximity reduces longitudinal gradients, hence the total response. Fig. 13 presents the case of two photons placed at various distances: the response is the maximum, at twice that of SPR (linear summation), when the two activated discs are 400 discs apart, and reduces down to $\sim$90% of the maximum when the discs are adjacent (or when both photons are on the same disc); at that point, the 9.7% deviation from linear summation would become 'noticeable'. Of course, such a setting cannot be achieved experimentally (yet), as individual photons cannot be directed to impinge at specific locations.

In Fig. 14, responses of four dim flashes ($\Phi = 11, 23, 45, 94$) are overlaid on Fig. 10 of [2] for comparison. As in Fig. 5, the rising phase, peak and tail agree well with the data, but the recovery is too steep, and steeper than in the bulk model (black curves in Fig. 14). This indicates that the feedback (calcium-modulated cyclase) mechanism built into the model is too strong at maximum calcium depletion, and/or other effects may be missing. Note that very low responses are produced if all the photons are taken to act on a single disc (or adjacent discs), and responses are too high if taken at maximum separation. By spreading the photons over discs at various distances, intermediate peak responses are obtained, and it is possible to match the experimental data, as seen in Fig. 14.

4 Discussion

The significance of this paper is its introduction of a mathematical technique that simplifies the computation of the spatio-temporal diffusion of second messengers in the well-understood visual transduction cascade. The layered geometry of the ROS presents significant computational difficulties in simulation of the diffusion of cGMP and Ca^{2+}. A full model that computes the process starting from Fick's law, set in the complex geometry of the rod outer segment, takes multiple days of computer time. A mathematical technique called homogenisation simplifies the geometry and allows the resulting partial differential equations to generate simulations in a few seconds on a desktop. The two models are compared in this paper and

Table 3: Spread of response at various times from single-photon activation. Both models produce same values for spread

Time	Spread interval $2\lambda_o$			Space constant λ_*	
ms	Number of discs	µm	% of ROS length	µm	% of ROS length
100	103	2.9	12.9	0.25	1.12
200	148	4.1	18.3	0.36	1.61
400	208	5.8	25.9	0.48	2.14
600	248	6.9	30.6	0.56	2.50
800	277	7.8	34.8	0.60	2.68
1000	297	8.3	37.0	0.61	2.72
1200	308	8.6	38.4	0.59	2.63
1400	308	8.6	38.4	0.55	2.46
1600	286	8.0	35.7	0.50	2.23
1800	166	4.6	20.5	0.42	1.87
2000	124	3.5	15.6	0.36	1.61

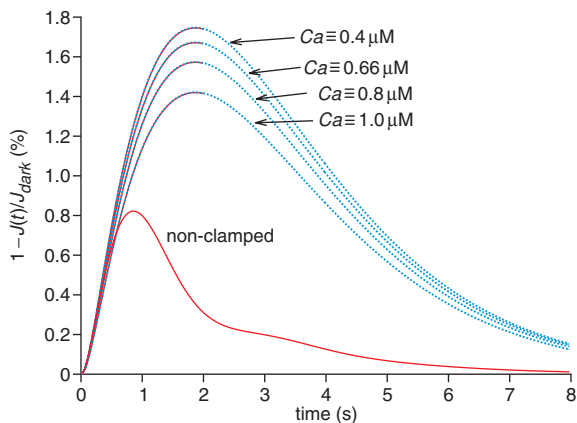130

IEE Proc.-Syst. Biol., Vol. 152, No. 3, September 2005

Fig. 10 *Clamped [Ca] simulations of single-photon response, for four different dark [Ca] concentrations [Ca]$_{dark}$ = 0.4, 0.66, 0.8, 1.0 μM*

Corresponding cGMP dark values are: $[cG]_{dark}$ = 6.1, 3.0, 2.4, 1.9 μM. For comparison, normal non-clamped case (of Fig. 2) is also shown (in red). Peak responses are much higher and occur later, and recovery is much slower than normal unclamped case. Maximum relative difference between full model and homogenised model values is less than 0.1%

are shown to have identical output to an accuracy of 0.03%. This simplified model is thus a simulation tool for biologists to predict the effect of various factors influencing the timing, spread and control mechanisms of this G protein-coupled receptor-mediated cascade.

4.1 Comparing simulations with experimental data

We have compared our simulations with experimental data for single-photon response in salamander rods. All parameters chosen were consistent with those published in [1, 2, 8, 16, 20, 21, 24], as described in Section 2.4, and are listed in Table 2. With these parameters, we obtained 0.54 pA (0.82%) peak reduction at 860 ms of the 66 pA dark current.

A simulation with rate constants as in [1] produced a very low response. Good agreement (Fig. 5) with measured salamander responses was obtained for D_{cG} = 100 μm^2 s^{-1}, v_{RE} = 195 s^{-1}, B_{cG} = 1, k_{cat}/K_m = 600, and B_{Ca} = 20. The amplitude of peak response is primarily regulated by

the value of v_{RE}, which was the last parameter value to be chosen.

We are currently devising a mathematical model, still based on homogenisation and concentrated capacity, that would account for one or several incisures. Note that the effect of incisures is implicitly incorporated in the various parameters of any bulk (well-stirred) model.

4.2 Single-photon response

The simulations of the single-photon response exhibit high localisation about the activation site. The local current $J(z_*, t)$, across the plasma membrane of the activated disc, depletes much more (14.8%, Fig. 6) than the total current $J(t)$ (0.82%).

It has been suggested that, in response to a single photo-isomerisation, [Ca], at the site of photon absorption, could drop to one-third of its resting value within 2 s ([2], page 249). Our simulations show a drop less than half as large (13%), within half the time ($\sim$1 s), under the activation mechanism of Section 2.2.3. A larger drop might occur if a more refined activation mechanism were employed, and if the effect of incisures was taken into account.

4.3 Multiple-photon response

Rod photoreceptors work over a large range of light intensities, and it is natural to ask to what degree the response to many photons can be accounted for by the response to a single photon. This has been tested with the spatially resolved computational model, using seven photons, spread across the discs of a photoreceptor outer segment in different ways.

When the ROS is activated by seven photons, both the local and total responses are lowest if the photons activate the same disc and highest if they activate equispaced discs at largest mutual distance (Fig. 11). Thus the arrangement of activation sites also plays a major role, and it can contribute to variability of responses to dim light merely by how far apart photons happen to be absorbed. All this elucidates the highly local nature of the response. Moreover, Fig. 11*b* shows that no significantly larger response is obtained by more and more photons on the same disc. This can be understood by the saturation of the signalling machinery at a single disc that received multiple photons, and the independence of discs from each other if

Table 4: Summary of single photon results (Φ = 1) for normal and clamped [Ca]

| | Current | | | | [cG] | | | | [Ca] | | | |
| | | Peak response | | | | Maximum depletion | | | | Maximum depletion | | |
	Dark pA	pA	%	Time ms	Dark μM	μM	%	Time ms	Dark μM	μM	%	Time ms
total	66	0.54	0.82	860								
local		9.8	14.8	860	3	0.24	8	790	0.66	0.085	12.8	1060
total	247	4.3	1.7	1880								
local		49	20	1300	6.08	0.67	11	1300	0.4		clamped	
total	66.3	1.1	1.7	1880								
local		12.6	19	1300	3	0.33	11	1300	0.66		clamped	
total	44.5	0.7	1.6	1880								
local		8	17.9	1300	2.38	0.26	11	1300	0.8		clamped	
total	31.3	0.44	1.4	1880								
local		5.1	16.2	1300	1.9	0.21	11	1300	1.0		clamped	

Local values for current, [cG] and [Ca] are those at lateral boundary at activated disc, i.e. $J(z, t)$, $[cG](z_*, t)$, $[Ca](z_*, t)$
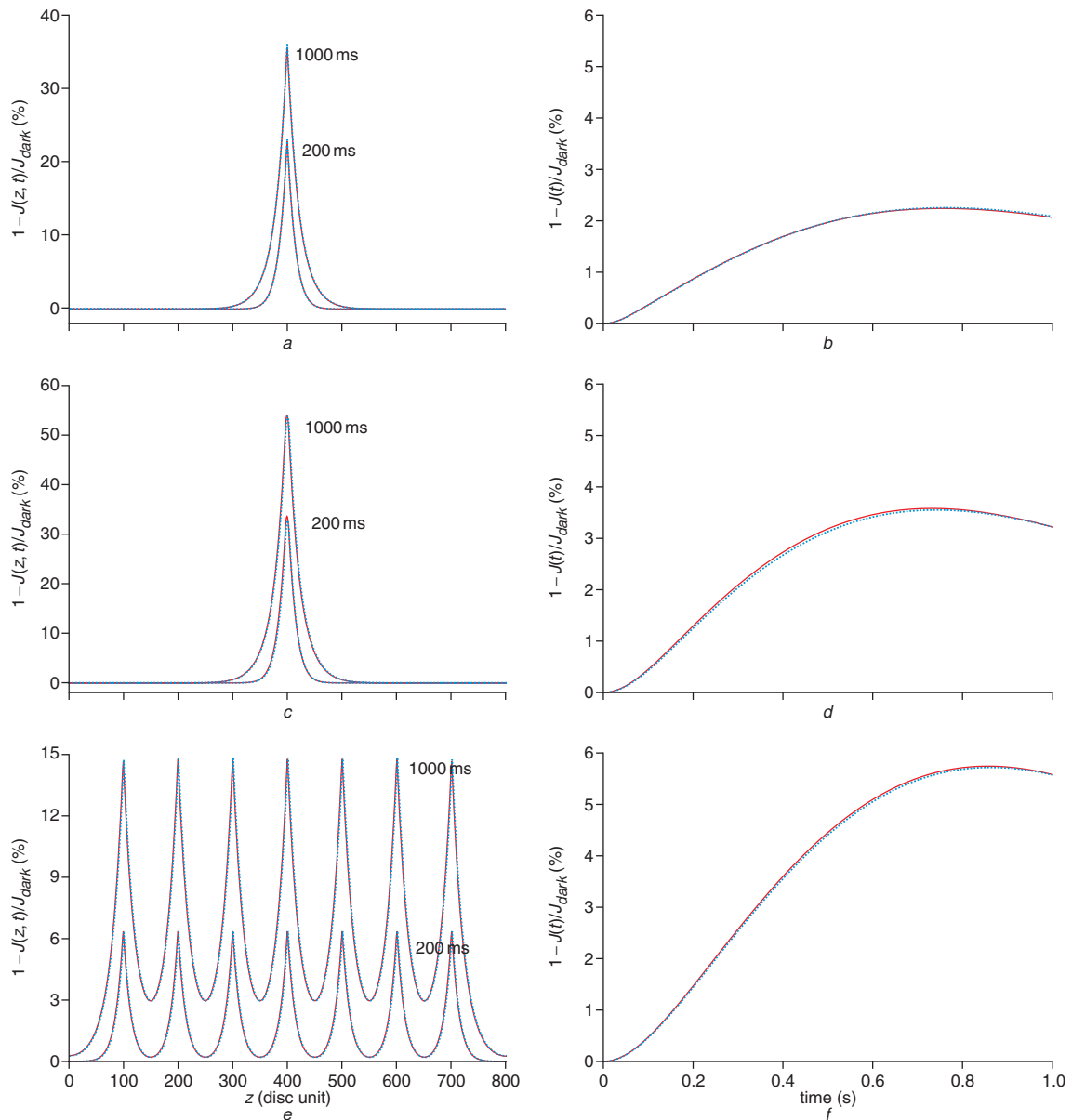
IEE Proc.-Syst. Biol., Vol. 152, No. 3, September 2005

131

Fig. 11 *Multiphoton simulations with $\Phi = 7$ photoisomerisations for three different arrangements of activation sites*

a, b, Only one disc is activated (disc 400) by 7 photons
c, d Seven adjacent discs are activated around centre of rod (discs 397–403), each by one photon
e, f Seven discs are activated, 100 discs apart from each other (discs 100, 200, 300, 400, 500, 600, 700)
a, c and *e* z-profiles of (local) relative response $1 - J(z, t)/J_{dark}$ at two times
b, d and *f*: Total response $1 - J(t)/J_{dark}$ against time
Suppression of circulating current varies considerably with arrangements of activated discs
Maximum relative difference between red (full model) and blue (homogenised): *a* 2.00% at 200 ms, 1.82% at 1000 ms; *c* 1.21% at 200 ms, 0.02% at 1000 ms; *e* 1.66% at 200 m, 1.20% at 1000 mss; *b* 0.58%; *d* 0.68%; *f* 0.01%

they are distant enough to not be within the area of 'spread' from another activated disc. Thus this model can account for the overall saturation of rod responses as the light intensity (number of photons impinging on each disc) increases.

4.4 On the spread of activation

The literature contains several notions of 'spread' [7–9] in terms of the diffusion coefficient of cGMP and various reaction parameters. Although they are all based on the assumption that the ROS is well-stirred in the transverse variables, they all build on different dynamic assumptions and lead to quite different estimates. For example, in [9], the spread length constant is defined as

$$\lambda_{HK} = \sqrt{D_{cG;eff} t_{peak}} \tag{40}$$

In [7], it is defined as

$$\lambda_{LM} = 0.554 \sqrt{D_{cG;eff} t_{peak}} \tag{41}$$

and, in [8], it is defined as

$$\lambda_{GK} = \sqrt{\frac{D_{cG;eff} t_{peak}}{r(1 + 6q)}} \quad \text{where } r(1 + 6q) \simeq 7\text{s}^{-1} \tag{42}$$

where r is the '... turnover rate in darkness of the free pool of cGMP' and q is 'the influence of Ca^{2+} on cGMP turnover rate' [8].

We have collected in Table 6 the values of λ_{HK}, λ_{LM} and λ_{GK}, for some of the values of $D_{cG;eff}$ in the published ranges indicated in Section 2.4.1.

As seen in Table 6, for the same value of longitudinal effective diffusion coefficient $D_{cG;eff}$, the three formulae

132

IEE Proc.-Syst. Biol., Vol. 152, No. 3, September 2005

Table 5: Summary of multi-photon results ($\Phi = 7$) for three different configurations discussed in Section 3.4 and **Fig. 11**

| | Current | | | | [cG] | | | | [Ca] | | | |
| | | Peak response | | | | Maximum depletion | | | | Maximum depletion | | |
	Dark pA	pA	%	Time ms	Dark μM	μM	%	Time ms	Dark μM	μM	%	Time ms
on one disc												
total	66	1.4	2.1	760								
local		24.7	37.2	700	3	0.63	24.2	520	0.66	0.21	31.6	960
on adjacent												
total	66	2.4	3.6	740								
local		37.9	57.4	670	3	1.1	36.2	650	0.66	0.32	48.9	920
100 discs apart												
total	66	3.8	5.7	860								
local		9.8	14.8	810	3	0.24	8.0	800	0.66	0.086	13	1070

(40)–(42) produce quite different 'spread' estimates, varying by almost a factor of 3. We have been unable to find in the literature any attempts to reconcile these notions and estimates.

Our approach to the notion of spread is computational and based on estimating those regions where the response is detectable.

The peak response of 0.54 pA we obtained for salamander rods is below the range 0.7–1.7 pA reported in [10] (p. 631) for single-photon activation in toad rods. In that paper, 5% suppression of the (30 pA) dark current was measured. From this, it is inferred [7, 13] that the change in [cG] effected by a single isomerisation must spread longitudinally over at least the corresponding fractional length of the outer segment. Lamb *et al.* [7] note (from 1 pA peak reduction of 30 pA dark current) that each photo-isomerisation affects at least $1/30$ (~ 2 μm or 3%) of the toad rod. The spread would be greater if the local response did not close all available cGMP-gated channels.

In rat rods, [27] estimated the spread of activation to be about 12 μm, or 20% of the rat rod (60 μm length). Again, it is not clear in what sense the notion of 'spread' is meant.

In Gecko lizard rods, Grey-Keller *et al.* [8] obtained a space constant of $\lambda_* \simeq 3.8$ μm. For salamander, we obtained

interval of detectable response $\lambda_o = 8.7$ μm, which amounts to 39% of ROS length (22.4 μm), and space constant $\lambda_* = 0.6$ μm (Table 3). The space constant appears to be much smaller than the value for lizard reported in [8]. However, the various spread results are not directly comparable, as they pertain to different species, they are often indirectly deduced, and the notion of 'spread' is vague and ill-defined in the literature. The cutoff we used for determining the maximum spread interval (0.1% of the dark current) is probably more strict than that of others, but realistic in view of the shape of the profiles. For example, a slightly higher cutoff 0.3% would produce ~ 7.4 μm (263 discs) spread interval, 15% narrower than from the 0.1% cutoff.

The previous discussion points out the difficulty in attempting any reasonable comparison with published notions and estimates of 'spread'. The only direct experimental work we are aware of is that of [8] for the gecko. With an exponential fitting of their experimental response curves, such as the one leading to λ_* in (10), they found $\lambda_* \simeq 3.8$ μm. Their theoretical analysis leading to (42) for $D_{cG;eff} \simeq 60$ μm^2 s^{-1} yields $\lambda_* \simeq 2.9$ μm, as indicated in Table 6. Our simulations were carried out with $D_{cG} = 100$ μm^2 s^{-1}, which, for $(f_A/f_V) \simeq 0.04$ and no viscosity and buffering effects, would correspond to
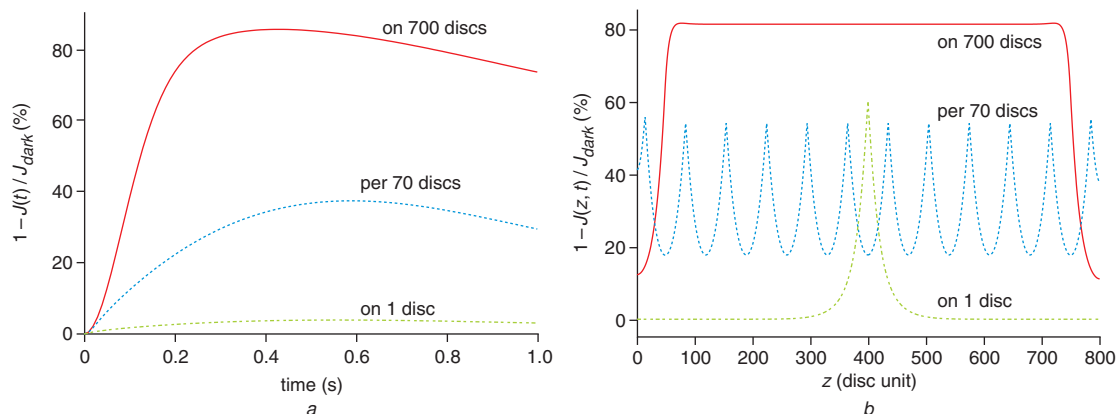

Fig. 12 *Multiphoton simulations with $\Phi = 700$ photoisomerisations for three different arrangements of activation sites, to illustrate dramatic effect of photon distribution (see Section 3.4)*

Case 1 (green curves): all 700 photons on one disc (disc 400)
Case 2 (blue curves): on 12 discs located 70 discs apart (discs 15, 85, ..., 785)
Case 3 (red curves): one photon on each of 700 consecutive discs (discs 50–749)
a Total response $1 - J(t)/J_{dark}$ against time. Peak response is only 4% in case 1, but 38% in case 2, and 86% in case 3. Other arrangements can generate essentially any intermediate response
b z-profiles of (local) relative response $1 - J(z, t)/J_{dark}$ at time 1000 ms for each of three cases in *a*
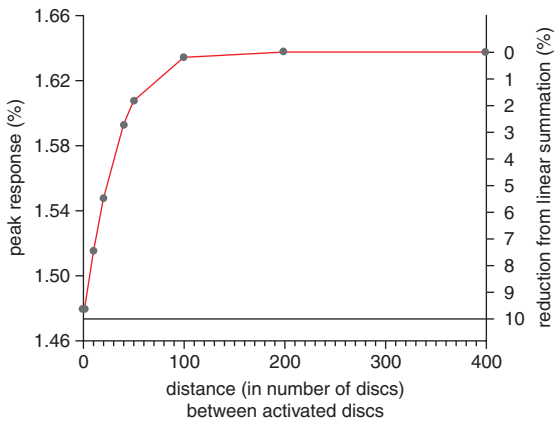
Fig. 13 *Two-photon simulations ($\Phi = 2$) exhibiting non-linear summation of SPRs as distance between activated discs decreases*

Left scale shows peak total response as % of J_{dark}; right scale shows deviation from linear summation as % of maximum relative response, against distance in disc units. When two photons are sufficiently far apart (at least 300 discs), (total) response is maximum (1.64%) at twice the SPR (0.082%); thus their effect is additive. This linear summation of SPRs begins to diminish at ~150 discs apart, as their spreads begin to overlap. Deviation becomes 9.7% when two photons act on adjacent discs or on same disc, where response is minimum (1.48%). Simulations were performed for distances of 0, 1, 10, 20, 40, 50, 100, 200, 400 discs apart, centred about middle (400th disc) of ROS. Peak times range from 830 to 860 ms

$D_{cG;eff} \simeq 4~\mu m^2~s^{-1}$. This value of $D_{cG,eff}$ is incomparable with $D_{cG;eff} \simeq 60~\mu m^2~s^{-1}$ taken in [8]. On the other hand, in Section 2.4.1, we have also pointed out that $D_{cG;eff} \simeq 60~\mu m^2~s^{-1}$ seems to contradict the accepted value of aqueous diffusivity of cGMP.

Another source of discrepancy between our value of λ_* and that of [8] is the issue of incisures. These naturally favour longitudinal diffusion of cGMP, thus resulting in larger spread.
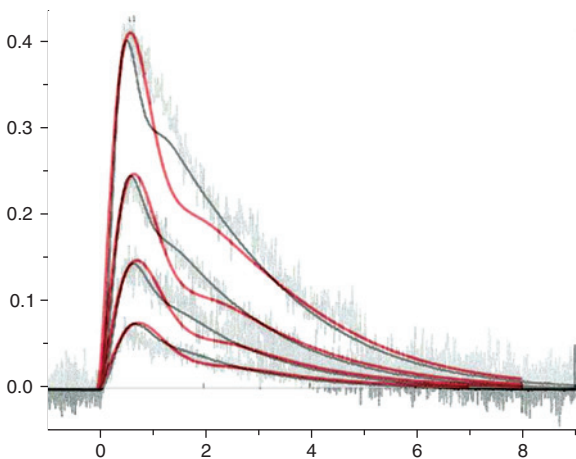

Fig. 14 *Comparison of responses for $\Phi = 11, 23, 45, 94$ photo-isomerisations with those in Fig. 10 of [2]. Flash responses of salamander rod (replotted from Fig. 12 of [20])*

Black curves are predictions from bulk model of [2]
Red curves are from our spatio-temporal model, obtained by following arrangements of activated discs: for $\Phi = 11$: 11 discs activated, lying 20 discs apart from each other (discs 300, 320, ..., 500); for $\Phi = 23$: 23 discs activated, 16 discs apart (discs 216, ..., 568); for $\Phi = 45$: 45 discs activated, 10 discs apart (discs 175, ..., 615); for $\Phi = 94$: 94 discs activated, 6 discs apart (discs 118, ..., 676). Different arrangements can produce quite different peak responses for each Φ, similar to $\Phi = 700$ case seen in Fig. 12

Table 6: Values of space constants against effctive diffusion coefficient $D_{cG;eff}$ predicted from (40)–(42)

$D_{cG;eff}$, $\mu m^2~s^{-1}$	λ_{HK}, μm	λ_{LM}, μm	λ_{GK}, μm
1.7	1.3	0.7	0.5
11	3.3	1.83	1.2
18.5	4.3	2.38	1.6
30	5.4	3.03	2.1
60	7.7	4.3	2.9

4.5 Homogenised against full model and locality

The maximum relative difference between the values produced by the homogenised and full models, for $[cG](z_*, t)$ and $[Ca](z_*, t)$, at the plasma membrane, at the activation level z_*, is about 0.19% (Fig. 3). Precisely, denoting by $[cG]^{full}$ and $[cG]^{hom}$, respectively, the computation of $[cG]$ by the full and homogenised models,

$$[cG]^{full}(z_*, t) - [cG]^{hom}(z_*, t) \simeq 0.19\%~[cG]^{full}(z_*, t)$$

The analogous relative difference for $[Ca](z_*, t)$ is 0.05%. Computing the corresponding currents from (3) and (4) at peak time, we find

$$J^{full}(z_*, t) - J^{hom}(z_*, t) \simeq 0.34\% \cdot J^{full}(z_*, t)$$

On the other hand, the difference between the total (averaged over the plasma membrane) currents $J^{full}(t)$ and $J^{hom}(t)$ normalised by $J^{full}(t)$ is less than 0.0002%. This indicates that the discrepancy arises only from a small region about the activation site and suggests that the homogenised model could be further improved by modifying the limiting process about the activation site. The discrepancies between the full and the homogenised model mentioned above are much smaller than typical experimental errors. Moreover, a simulation of 8 s with the (axisymmetric) full model and parallel computing required over 100 h, whereas the corresponding computation with the homogenised model took only 300 s on a desktop (Section 3.1).

Simulations could be carried out for non-axisymmetric phenomena, and, in such a case, the response and 'spread' would depend on the eccentric activation site (Section 2.1.4).

Finally, the simulations are in remarkable agreement with the experimental results shown in Fig. 5.

All this points to the homogenised model as a *building block* in modelling diffusion of second messengers in the layered geometry of the cytosol of the ROS. Some improvements and expansions are possible. These include refining the homogenised/concentrated limit near the activation site, a mathematical account of incisures, and the activation and recovery mechanisms. The theoretical grounding of this machinery is sufficiently robust to allow for improvements/ modifications within its logical structure.

4.6 Homogenisation methods

Homogenisation methods have been successfully used in physical processes where it is possible to identify a periodic geometry, and their success relies on a careful mathematical analysis of the underlying geometry. In the case of visual transduction, its application was made possible by the layered structure of the discs.

In other signalling processes, the structure of the cytoplasm is not periodic, and the actin cytoskeleton exhibits a random structure. In general, cells do not have a periodic structure, nor a natural notion of surface-to-volume

134

IEE Proc.-Syst. Biol., Vol. 152, No. 3, September 2005

interaction. The classical homogenisation theory has very recently been applied to investigate limiting processes across randomly distributed scales [28]. We feel that these biological processes could be attacked by these new ideas, and, in turn, they could provide motivation and experimental validation to further the theory of diffusion in randomly organised media.

5 Conclusions

A spatio-temporal model for diffusion of second messengers in rod phototransduction has been presented, and a consistent set of parameters have been determined for the model to predict single-photon response in good agreement with experimental data. The model exhibits strong localisation of the response about the activation site and enables us to quantify the longitudinal spread at any particular time (item 3 of Section 3.2 and Table 3). We also noticed an interesting dependence of response on the arrangement of activation sites (Section 3.4), namely that maximum separation of activated sites produces maximum response, which by itself can create variability of dim light responses apart from any other factors.

Given a set of parameters, our model can be used to determine the spatial and temporal variation of the concentrations of the second messengers cGMP and Ca^{2+} and of the resulting electrical response, providing detailed information that may be diffcult to obtain experimentally. It makes possible computational experiments for the interpretation of available biological data, comparison of model predictions with measurements, determination of sensitivity of output on various model parameters, and the design of further biological experiments. It can also be used for determining physical parameter values that are difficult, non-feasible or impossible to measure directly. In addition, it can be used to simulate phototransduction in rods of various sizes (longer or thinner and/or of variable cross-section).

In summary, this mathematical tool allows investigation into the space-time, local behaviour of signalling using second messengers in the ROS.

The control of signal transduction in cells occurs by precise, highly regulated localisation of key enzymes in sub-compartments in cells. Homogenisation methods such as those described here may, in the future, be applied to the complex geometries of other cell types, allowing precise modelling of the particular spatial locations in cells of the components of signalling pathways, as well as their spatial and temporal evolution, a dramatic improvement from current models based upon ordinary differential equations. It should be possible to use this approach to build up a realistic spatio-temporal signal transduction network to test specific hypotheses of signal cross-talk, integration and decision-making.

6 Acknowledgments

7 References

1　Nikonov, S., Lamb, T.D., and Pugh, E.N. Jr.: 'The role of steady phosphodiestarase activity in the kinetics and sensitivity of the light-adapted salamander rod photoresponse', *J. Gen. Physiol.*, 2000, **116**, pp. 795–824

2　Pugh, E.N. Jr., and Lamb, T.D.: 'Phototransduction in vertebrate rods and cones: molecular mechanisms of amplification, recovery and light adaptation', *in* Stavenga, D.G., Degrip, W.J. and Pugh, E.N. Jr. (Eds.): 'Molecular mechanism in visual transduction' (Elsevier, Amsterdam, 2000), pp. 183–255

3　Andreucci, D., Bisegna, P., and DiBenedetto, E.: 'Homogenisation and concentrated capacity for the heat equation with non linear variational data in reticular almost disconnected structures and applications to visual transduction', *Annali di Mat Pura et Appl*, 2003, **4**, pp. 375–407

4　Andreucci, D., Bisegna, P., Caruso, G., Hamm, H.E., and DiBenedetto, E.: 'Mathematical model of the dynamics of second messengers in visual transduction: homogenisation and concentrated capacity', *Biophysical J.*, 2003, **85**, pp. 1358–1376

5　Khanal, H., Alexiades, V., DiBenedetto, E., and Hamm, H.E.: 'Numerical simulation of diffusion of second messengers cGMP and Ca^{2+} in rod photoreceptor outer segment of vertebrates', *in* Bezrukov, S.M. (Ed.): 'Unsolved problems of noise and fluctuations: UPoN 2002'. AIP Conference Proceedings 665, American Institute of Physics, 2003, pp. 165–172

6　Khanal, H., Alexiades, V., and DiBenedetto, E.: 'Response of dark-adapted retinal rod photoreceptors', *in* Sambandham, M. (Ed.): 'Dynamic systems and applications 4' (Dynamic Publishers, 2004), pp. 138–145

7　Lamb, T.D., McNaughton, P.A., and Yau, K.-W.: 'Spatial spread of activation and background desensitisation in toad rod outer segment', *J. Physiol.*, 1981, **318**, pp. 463–496

8　Gray-Keller, M., Denk, W., Shraim, B., and Detwiler, P.B.: 'Longitudinal spread of second messenger signals in isolated rod outer segments of lizards', *J. Physiol.*, 1999, **519**, pp. 679–692

9　Holcman, D., and Korenbrot, J.I.: 'Longitudinal diffusion in retinal rod and cone outer segment cytoplasm: the consequence of cell structure', *Biophysical J.*, 2004, **86**, (4), pp. 2566–2582

10　Baylor, D.A., Lamb, T.D., and Yau, K.-W.: 'The membrane current of single rod outer segments', *J. Physiol.*, 1979, **288**, pp. 589–611

11　Baylor, D.A., Lamb, T.D., and Yau, K.-W.: 'Responses of retinal rods to single photons', *J. Physiol.*, 1979, **288**, pp. 613–634

12　Matthews, G.: 'Spread of the light response along the rod outer segments; an estimate of the patch-clamp recordings', *Vision Res.*, 1986, **26**, pp. 535–541

13　Olson, A., and Pugh, E.N. Jr.: 'Diffusion coefficient of cyclic GMP in salamander rod outer segments estimated with two fluorescent probes', *Biophysical J.*, 1993, **65**, pp. 1335–1352

14　Stryer, L.: 'Visual excitation and recovery', *J. Biol. Chem.*, 1991, **226**, pp. 10711–10714

15　Dumke, C.L., Arshavsky, V.Y., Calvert, P.D., Bownds, M.D., and Pugh, E.N. Jr.: 'Rod outer segment structure influences the apparent kinetic parameters of cyclic GMP phospodiesterase', *J. Gen. Physiol.*, 1994, **103**, pp. 1071–1098

16　Koutalos, Y., Nakatani, K., and Yau, K.-W.: 'Cyclic GMP diffusion coefficient in rod photoreceptors outer segments', *Biophysical J.*, 1995, **68**, pp. 373–382

17　Rieke, F., and Baylor, D.A.: 'Origin of reproducibility in the responses of retinal rods to single photons', *Biophysical J.*, 1998, **75**, pp. 1836–1867

18　Rieke, F., and Baylor, D.A.: 'Single photon detection by rod cells of the retina', *Reviews Mod. Physics*, 1998, **70**, (3), pp. 1027–1036

19　Hamer, R.D.: 'Analysis of Ca^{++}-dependent gain changes in PDE activation in vertebrate rod phototransduction', *Molecular Vision*, 2000, **6**, pp. 265–286

20　Nikonov, S., Engheta, N., and Pugh, E.N. Jr.: 'Kinetics of recovery of the dark-adapted salamander rod photoresponse', *J. Gen. Physiol.*, 1998, **111**, pp. 7–37

21　Koutalos, Y., and Yau, K.-W.: 'Regulation of sensitivity in vertebrate rod photoreceptors by calcium', *Trends in Neurosciences*, 1996, **19**, pp. 73–81

22　Nakatani, K., Chen, C., and Koutalos, Y.: 'Calcium diffusion coefficient in rod photoreceptor outer segments', *Biophysical J.*, 2002, **82**, pp. 728–739

23　Lamb, T.D., and Pugh, E.N. Jr.: 'A quantitative account of the activation steps involved in phototransduction in amphibian photoreceptors', *J. Physiol.*, 1992, **449**, pp. 719–758

24　Leskov, I.B., Klenchin, V.A., Handy, J.W., Whitelock, G.G., Govardovskii, V.I., *et al.*: 'The gain of rod phototransduction: reconciliation of biochemical and electrophysical measurements', *Neuron*, 2000, **27**, pp. 525–537

IEE Proc.-Syst. Biol., Vol. 152, No. 3, September 2005

135

25 Norton, A.W., D'Amours, M.R., Grazio, H.J., Herbert, T.L., and Cote, R.H.: 'Mechanism of transducin activation of frog photoreceptor phosphodiesterase. Allosteric interactions between the inhibitory gamma subunit and the noncatalytic cGMP–binding sites', *J. Biol. Chem.*, 2000, **275**, (49), pp. 38611–38619

26 Pugh, E.N. Jr., and Lamb, T.D.: 'Amplification and kinetics of the activation steps in phototransduction', *Biochimica et Biophysica Acta*, 1993, **1141**, pp. 111–149

27 Hagins, W.A., Penn, R.D., and Yoshikami, S.: 'Dark current and photocurrent in retinal rods', *J. Physiol.*, 1970, **10**, pp. 380–412

28 Torquato, S.: 'Random heterogeneous materials' (Springer-Verlag, New York, 2002)

7 Appendices

7.1 Numerical simulations

Computational models have been developed for the full model introduced in Section 2.2 and for the corresponding homogenised model introduced in Section 2.3. The simulations are based, respectively, on finite volume and finite element discretisations and implemented in Fortran and Matlab, as described below.

The activation mechanism used for both models is the *lumped method* described in Section 2.2.3, which implies that the process is axially symmetric. Accordingly, axial symmetry is assumed in the simulations, reducing the computation to two dimensions, in the radial, r, and axial, z, directions.

The full model faithfully describes the physical problem; as such, it requires discretisation of the intricate microstructure of the rod, as explained in Appendix 2, leading to a highly refined mesh and, consequently, to very high computational cost. By contrast, the disc-free geometry of the homogenised model does not demand high resolution along the z-direction and can be resolved using a much coarser mesh, achieving essentially the same accuracy as the highly resolved full model. As described in greater detail in Section 3.1, the gradients of $[cG]$ and $[Ca]$ are concentrated locally near the activation site; thus the homogenised model can be efficiently implemented by using a very coarse z-mesh, which needs to be refined locally only near the activation site.

To assess the effectiveness of the homogenised model, numerical simulations from both models (full and homogenised) are compared in detail in Section 3.1. Further simulation results are presented in Section 3.

Because of axial symmetry, there is no angle dependence, and so, in particular, $J_{loc}(\theta, z, t) = J(z, t)$ and $[cG] = [cG](r, z, t)$ are functions of the radial, r, and axial, z, co-ordinates and of time t. If a quantity, e.g. $[cG]$, is computed on the outer membrane ($r = R_{rod}$ for full, $r = R$ for homogenised), in view of symmetry with respect to the axis of the ROS, we set

$$[cG]\big|_{outer\ membrane} = [cG](z, t)$$

Similar notation is adopted for the remaining variables, $[Ca]$, J_{cG}, etc.

The numerical solution of the partial differential equations gives the (discretised) spatial distribution of $[cG]$ and $[Ca]$ in the cytosol as they evolve in time. Then the local current $J_{loc}(z, t)$ at any level z at any time t is obtained from (3)–(6) using the values of $[cG](z, t)$ and $[Ca](z, t)$, on the outer membrane, at that level z and time t. The total current $J(t)$ across the entire plasma membrane at time t is the mean value of $J(z, t)$ over Σ_{rod} (see (7)). Results are presented in terms of the response $J_{dark} - J(t)$, relative (or normalised) response $1 - J(t)/J_{dark}$ and local normalised response $1 - J(z, t)/J_{dark}$.

7.2 Discretisation of full model

The numerical solution of the full model is based on finite volume discretisation of the partial differential equations and boundary conditions for the axially symmetric case. The domain to be discretised here is a rod Ω_{ε_o} containing $n = 800$ discs, each of thickness ε_o (=14 nm). Axisymmetric finite volumes have been employed to create the mesh. We partition the rod into n small cylinders, which we will call disc units, each of height

$$h_i = \frac{1}{2}v\varepsilon + \varepsilon + \frac{1}{2}v\varepsilon \quad i = 1, 2, \ldots, n$$

containing one disc in its middle. Each disc unit is discretised by subdivision of its radius and its height into subintervals and rotation about the z-axis. Thus each finite volume is an annulus of rectangular cross-section. Concentrations are approximated by their mean values over each finite volume. By integration of the partial differential equations (11) over each finite volume, local balance equations are written for each volume that express mass conservation at the discrete level, just as the diffusion equations express mass conservation at the continuous level.

Time-integration is performed by explicit time-stepping (most convenient for parallel computation), with time-steps sufficiently small to ensure numerical stability of the scheme; however, boundary values are updated implicitly by direct solution of the resulting equations.

Parallelisation: Owing to the intricate geometry of the cytosol, even the axisymmetric version of the full model involves very intensive computations. To reduce the computation time, we parallelised the scheme for distributed memory clusters of processors, using domain decomposition by assigning groups of disc units to processors. The parallel implementation employs the message passing interface (MPI) library, following the master/slaves paradigm generated in single program multiple data (SPMD) mode, where one processor acts as a master and the rest as slaves. The master handles input/output, distributes tasks to the slaves, and controls and synchronises them. The slaves all solve the same problem (but on their own segment of the mesh), exchange boundary values with their neighbours through message passing, and send their output to the master.

In the simulations reported here, we employ a fairly fine grid in each disc unit, consisting of 32 r-nodes in $[0, R]$; two r-nodes in $R_{rod} - R$; one z-node below the disc, two z-nodes along the height of each disc, and one node above the disc. Thus each disc unit is discretised into $34 \times 4 = 136$ control volumes, resulting in $136 \times 800 = 108\,800$ control volumes for a typical rod with 800 discs. Finer grids were tested, with no discernible effect (to at least three significant digits).

Computations were performed on four networked Intel dual Xeon workstations. A typical 1000 ms simulation for a rod with 800 discs with such a grid, using four dual processors (eight slave processes), takes about 13 h.

7.3 Discretisation of homogenised model

The numerical solution of the homogenised model is based on finite element discretisation of the weak form of the homogenised-model equations (26)–(27), for the axially symmetric case. The domain to be discretised consists of the cylinder Ω (the limiting ROS), the zero-thickness disc $\mathcal{D}_R \times \{z_*\}$ (at the activated face F_{j*}^-) and the lateral surface S (the limiting outer shell).

136

IEE Proc.-Syst. Biol., Vol. 152, No. 3, September 2005

In the homogenised model, the disc unit containing an activated face is reduced, through a capacity-concentration process, to $\mathcal{D}_R \times \{z_*\}$. Accordingly, the volume equivalent to a disc unit just above the activated level is no longer available for diffusion, as it has been concentrated on the surface $\mathcal{D}_R$. We compensate for this in the discretisation by removing a slit of thickness of one disc unit from the volume just above z_*. The location z_* is the z co-ordinate of the activated face F_*^-.

An axisymmetric finite-element mesh is created by rotating an $r-z$ mesh about the z-axis. The $r-z$ mesh consists of three-node isoparametric elements of triangular cross-section for the interior of the rod; circular-annular elements for the activated disc; and two-node surface-cylindrical elements for the outer surface. For a non-axisymmetric activation mechanism, a more complicated mesh must be adopted, using four-node tetrahedral elements for the interior of the rod and three-node triangular elements for the activated disc and the outer shell [3].

Linear shape functions are used to interpolate (nodal values of) the solution in the interior of each element. As a consequence, both $[cG]$ and $[Ca]$ are approximated by continuous functions. As the greatest rates of change of $[cG]$ and $[Ca]$ occur near the activated disc, a mesh-generation algorithm has been written to produce a finer z-mesh in a chosen region around the activated disc. This enables us to obtain an accurate solution using far fewer elements, thereby considerably reducing the computational cost.

Time-integration was performed with the Crank–Nicolson scheme, which guarantees stability and convergence without requiring time steps that are too small. The non-linear forcing terms have been linearised within each finite element about the local mean value of $[cG]$ and $[Ca]$, evaluated at the middle of the time-step (midpoint between the old and new time), as prescribed by the semi-implicit integration method. Accordingly, an iterative procedure is necessary to advance the solution to the new time, for which we use a Matlab linear system solver.

The finite-element scheme has been implemented by a dedicated code within the Matlab environment. To reduce the computational time, the evaluation of the non-linear forcing terms needed at each time-step is performed by a routine written in C, which, after compilation with the 'mex' compiler of Matlab, is used in the code as a Matlab function.

Several numerical tests were performed to find out the most economical grid size and time-step for which the scheme attains convergence. Some of those tests are reported in Table 7 in terms of peak response, but similar convergence was achieved also for all other significant quantities of the problem. The last column shows the CPU time for 1 s simulation.

The numerical tests in Table 7 show that a 16×120 mesh (with finer z-grid near the activated disc) and time step of 10 ms are sufficient for simulations, and it runs very fast. Indeed, refinement of the grid both in the radial and axial directions does not lead to any significant change in the solution.

Table 7: Effect of mesh size on peak response value and CPU time in homogenised model, for 1 s simulation, using time-step of 10 ms

$r \times z$ mesh	Peak response %	CPU time, s
64×240	0.81964	885
32×400	0.81967	613
16×720	0.81986	506
16×240	0.81991	118
16×120	0.81993	53

IEE Proc.-Syst. Biol., Vol. 152, No. 3, September 2005

137